Available online www.jsaer.com

***Journal of Scientific and Engineering Research*, 2018, 5(5):395-430**

Research Article

ISSN: 2394-2630
CODEN(USA): JSERBR

Spectral Method Applied to Turbulent Chemical Non-Equilibrium Reentry Flows in 2D – Five Species

Edisson Sávio de Góes Maciel

Rua Santa Clara, 245 – Cx. Postal: 2029 – 12.243-970 – São José dos Campos – SP – Brazil

Abstract In this work, a spectral method is applied to the Favre-averaged Navier-Stokes equations in two-dimensions, employing a structured spatial discretization, and using a conservative and finite volume approaches. Turbulence is taken into account considering the implementation of five k-ω two-equation turbulence models, based on the works of Coakley 1983; Wilcox; Yoder, Georgiadids and Orkwis; Coakley 1997; and Rumsey, Gatski, Ying and Bertelrud. The numerical experiments are performed using the Van Leer numerical algorithm. The Euler backward method is applied to march the scheme in time. The spectral method presented in this work employs collocation points and variants of Chebyshev and Legendre interpolation functions are analyzed. Chemical non-equilibrium is studied using a five species chemical model. The "hot gas" hypersonic flows around a blunt body, and around a reentry capsule, in two-dimensions, are simulated. The results have indicated that the Chebyshev collocation point variants are more accurate in terms of stagnation pressure estimations. In the blunt body problem such errors are inferior to 16.0%, being 2.66% the best result, while in the reentry capsule problem such errors are inferior to 8.0%, being 3.88% the best result. The Legendre collocation point variants are more accurate in terms of the lift coefficient estimations. Moreover, the Legendre collocation point variants are more computationally efficient and cheaper.

Keywords Spectral method, k-ω two equation models, Reentry flows, Favre-averaged Navier-Stokes equations, Chemical non-equilibrium, Five species chemical model, Van Leer scheme.

1. Introduction

There are several approaches for computationally modeling fluid dynamics. These include finite difference, finite element, and spectral methods to name a few. Finite element and finite difference methods are frequently used and offer a wide range of well-known numerical schemes. These schemes can vary in terms of computational accuracy but are typically of lower order of accuracy. If a more accurate solution is desired, it is common practice to refine the mesh either globally or in a region of interest. This can often be a complicated or time consuming process as global mesh refinement will greatly increase the computation time while local refinement requires an elaborated refinement operation [1].

Alternatively, polynomial refinement has been used to improve the solution accuracy and has been shown to converge more quickly than mesh refinement in some cases [2-3]. For finite difference methods, polynomial refinement is performed by including neighboring node values in a higher order polynomial [4]. This can increase the complexity of the scheme especially near the boundaries where nodes do not exist to construct the higher order polynomials. Finite element methods instead increase the number of unknown values within the cell itself to construct a higher order solution [5].

A scheme with a very high formal order of accuracy will not necessarily always produce the highest resolution. [6] demonstrated that a spectral-like scheme with a formal fourth-order accuracy produced a much more highly resolved solution than schemes with higher formal orders of accuracy when comparing modified wave numbers.

Therefore, formal order of accuracy does not provide a comprehensive basis for selecting the best solution procedure. State-of-art methods such as spectral methods fall into this category.

Spectral methods are considered a class of solution techniques using sets of known functions to solve differential equations [7]. Such methods are generally considered high order and capable of obtaining solutions with a high resolution. Unlike finite-difference and finite-element methods, spectral methods utilize an expansion in terms of global, rather than local, basis functions to represent the solution of a differential equation. When properly applied, these techniques accurately resolve phenomena on the scale of the mesh spacing. The order of truncation error decay with mesh refinement is also higher than which can be achieved with finite-difference and finite-element methods. For problems with smooth solutions, it is possible to produce spectral method whose truncation error goes to zero as faster than any finite power of the mesh spacing (exponential convergence).

Spectral methods may be viewed as an extreme development of the class of discretization schemes known by the generic name of method of weighted residuals (MWR) [8]. The key elements of the MWR are the trial functions (also called the expansion or approximating functions) and the test functions (also known as weighted functions). The trial functions are used as the basis functions for a truncated series expansion of the solution that, when substituted into the differential equation, produces the residual. The test functions are used to enforce the minimization of the residual.

The choice of the trial functions is what distinguishes the spectral methods from the element and finite difference methods. The trial functions for spectral methods are infinitely differentiable global functions (Typically, they are tensor products of the eigenfunctions of singular Sturm-Liouville problems). In the case of finite element methods, the domain is divided into small elements and a trial function is specified in each element. The trial functions are thus local in character and well suited for handling complex geometries. The finite difference trial functions are likewise local.

The choice of test function distinguishes between Galerkin and collocation approaches. In the Galerkin approach, the test functions are the same as the trial functions, whereas in the collocation approach the test functions are translated Dirac delta functions. In other words, the Galerkin approach is equivalent to a least-square approximation, whereas the collocation approach requires the differential equations to be solved exactly at the collocation points.

The collocation approach is the simplest of the MWR and appears to have been first used by [9] in his study of electronic energy bands in metals. A few years later, [10] applied this method to the problem of torsion in square prism. [11] developed it as a general method for solving ordinary differential equations. They used a variety of trials functions and an arbitrary distribution of collocation points. The work of [12] established for the first time that a proper choice of the trial functions and the distribution of collocation points are crucial to the accuracy of the solution. Perhaps he should be credited with laying down the foundation of the orthogonal collocation method.

Spectral methods have been used on one-dimensional, compressible flow problems with piecewise linear solutions by [13-14]. These reports demonstrated that spectral methods, when combined with appropriate filtering techniques, can capture one-dimensional shock waves in otherwise featureless flows. A different sort of demonstration was provided by [15]. They exhibited spectral solutions of compressible flows with nontrivial structures in the smooth regions.

Renewed interest in the area of hypersonic flight has brought computational fluid dynamics (CFD) to the forefront of fluid flow research [16]. Many years have seen a quantum leap in advancements made in the areas of computer systems and software which utilize them for problem solving. Sophisticated and accurate numerical algorithms are devised routinely that are capable of handling complex computational problems. Experimental test facilities capable of addressing complicated high-speed flow problems are still scarce because they are too expensive to build and sophisticated measurements techniques appropriate for such problems, such as the non-intrusive laser, are still in the development stage. As a result, CFD has become a vital tool, in some cases the only available tool, in the flow research today.

The study of hypersonic flows has gained momentum with the advent of concepts like the National AeroSpace Plane (NASP) and similar trans-atmospheric vehicles. Under the very high velocity and temperature conditions

experienced by hypersonic vehicles, departure from chemical and thermal equilibrium occurs. Properties of air change dramatically as new chemical species are produced at the expense of others. The simple one temperature model used to describe the energy of air becomes inapplicable, and it becomes necessary to consider one or more additional temperatures (corresponding to vibrational and electronic energies). Determination of aerothermal loads on blunt bodies in such an environment is of great importance.

In high speed flows, any adjustment of chemical composition or thermodynamic equilibrium to a change in local environment requires certain time. This is because the redistribution of chemical species and internal energies require certain number of molecular collisions, and hence a certain characteristic time. Chemical non-equilibrium occurs when the characteristic time for the chemical reactions to reach local equilibrium is of the same order as the characteristic time of the fluid flow. Similarly, thermal non-equilibrium occurs when the characteristic time for translation and various internal energy modes to reach local equilibrium is of the same order as the characteristic time of the fluid flow. Since chemical and thermal changes are the results of collisions between the constituent particles, non-equilibrium effects prevail in high-speed flows in low-density air.

In chemical non-equilibrium flows the mass conservation equation is applied to each of the constituent species in the gas mixture. Therefore, the overall mass conservation equation is replaced by as many species conservation equations as the number of chemical species considered. The assumption of thermal non-equilibrium introduces additional energy conservation equations – one for every additional energy mode. Thus, the number of governing equations for non-equilibrium flow is much bigger compared to those for perfect gas flow. A complete set of governing equations for non-equilibrium flow may be found in [17-18].

In spite of the advances made in the area of compressible turbulence modeling in recent years, no universal turbulence model, applicable to such complex flow problems has emerged so far. While the model should be accurate it should also be economical to use in conjunction with the governing equations of the fluid flow. Taking these issues into consideration, k-ω two-equation models have been chosen in the present work [19-23]. These models solve differential equations for the turbulent kinetic energy and the vorticity. Additional differential equations for the variances of temperature and species mass fractions have also been included. These variances have been used to model the turbulence-chemistry interactions in the reacting flows studied here.

In the current work, a spectral method is applied to the Favre-averaged Navier-Stokes equations, employing structured spatial discretization, and using a conservative and finite volume approaches. Turbulence is taken into account considering the implementation of five k-ω two-equation turbulence models, based on the works of [19-23]. The numerical algorithm of [24] is used to perform the reentry flow numerical experiments, which give us an original contribution to the CFD community. The Euler backward method is applied to march the scheme in time. The spectral method presented in this work employs collocation points and variants of Chebyshev and Legendre interpolation functions are analyzed. The "hot gas" hypersonic flows around a blunt body and around a reentry capsule, in two-dimensions, are simulated. The convergence process is accelerated to steady state condition through a spatially variable time step procedure, which has proved effective gains in terms of computational acceleration [25-26]. The reactive simulations involve Earth atmosphere chemical model of five species and seventeen reactions, based on the [27] model. N, O, N_2, O_2, and NO species are used to perform the numerical comparisons. The results have indicated that the Chebyshev collocation point variants are more accurate in terms of stagnation pressure estimations. In the blunt body problem such errors are inferior to 16.0%, being 2.66% the best result, while in the reentry capsule problem such errors are inferior to 8.0%, being 3.88% the best result. The Legendre collocation point variants are more accurate in terms of the lift coefficient estimations. Moreover, the Legendre collocation point variants are more computationally efficient and cheaper.

2. Spectral Method

Two classes of techniques for spectral discretization are referred to as tau and collocation methods [28]. The latter technique is used here. In this scheme, the approximation series is determined by satisfying the differential equation exactly at a set of distinct collocation points. The locations of these points in the domain are linked to the choice of basis function. In this study, arbitrary collocation points are implemented. The collocation method is used here since enforcement of boundary conditions and evaluations of nonlinear terms are straightforward. Additionally, some accuracy advantage is seen in the collocation method over the tau method for a number of problems [28]. The series expansion for a function Q(x) may be represented as

$$Q_N(x) = \sum_{n=0}^{N} \hat{Q}_n B_n(x), \quad (1)$$

where $B_n(x)$ are the basis functions and N is the total number of nodes employed in the interpolation process (it is also the order of accuracy of the spectral method). The coefficients $\hat{Q}_n$ are often termed the spectrum of $Q_N(x)$. One common technique used to evaluate the spectrum is to consider Eq. (1) as an interpolation series representing Q(x). The interpolation "nodes" of such series are the collocation points of the method. For a scheme based on Chebyshev collocation, the basis functions are:

$$B_n(x) = T_n(x) = 2xP_{n-1}(x) - P_{n-2}(x), n \geq 2, \quad (2)$$

with: $P_0(x) = 1$ and $P_1(x) = x$. The Chebyshev-Gauss-Lobatto standard collocation points are

$$x_l = \cos\left(\frac{\pi l}{N}\right), \qquad l = 0, 1, \ldots, N. \quad (3)$$

The Chebyshev collocation points result from a simple change of variables, which relates the Chebyshev interpolation series to a Fourier cosine series [28]. To evaluate the $\hat{Q}_n$, the inverse relation is required. This is

$$\hat{Q}_n = \hat{c}_n \sum_{l=0}^{N} w_l B_n(x_l) Q_{i,j}, \qquad n = 0, 1, \ldots, N, \quad (4)$$

with w_l being a normalized weighting function and $\hat{c}_n$ a constant. These variables assume the following expressions to a Chebyshev interpolation:

$$\hat{c}_n = \frac{2}{N\bar{c}_n}, \text{ where: } \bar{c}_n = \begin{cases} 2, & n = 0 \text{ or } N \\ 1, & 1 < n < N-1 \end{cases}; \text{ and } w_l = \frac{1}{\bar{c}_l}. \quad (5)$$

Legendre collocation is based on using Legendre polynomials as the basis function in Eq. (1), e.g.,

$$B_n(x) = \left[(2n-1)xP_{n-1}(x) - (n-1)P_{n-2}(x)\right]/n, \qquad n \geq 2, \quad (6)$$

where: $P_0(x) = 1$ and $P_1(x) = x$. Interpolation via Legendre series cannot easily be related to trigonometric interpolation, so there is no simple expression to evaluate the $\hat{Q}_n$ coefficients. Appeal must be made to the theory of numerical quadrature to form an approximation to the integrals which result from analytic Legendre interpolation [29]. Considering Eq. (4), the normalized weights and constant of the Legendre-Gauss-Lobatto collocation points are

$$w_l = \frac{1}{N(N+1)B_N^2(x_l)} \quad \text{and} \quad \hat{c}_n = \begin{cases} 2n+1, & n = 0,1,\ldots,N-1 \\ N, & n = N \end{cases}. \quad (7)$$

In this work, it was assumed that the Legendre-Gauss-Lobatto collocation points are the same as the Chebyshev-Gauss-Lobatto ones. It was also adopted the following collocation points and normalized weights for the Chebyshev-Gauss-Radau interpolation, based on the work of [30]:

$$x_l = \cos\left(\frac{2\pi l}{2N+1}\right), \quad (8)$$

$$w_l = \begin{cases} \frac{N}{2N+1}, & l = 0 \\ \frac{N}{N+1}, & \text{elsewhere} \end{cases}. \quad (9)$$

For the Legendre-Gauss-Radau interpolation, also based in [30], the collocation points are defined by Eq. (8) and the normalized weights are described by:

$$w_l = \begin{cases} \frac{1}{(N+1)^2}, & l = 0 \\ \frac{1}{2(N+1)^2} \times \frac{1-x_l}{B_N(x_l)}, & \text{elsewhere} \end{cases}. \quad (10)$$

The same calculation to the vector of conserved variables Q is applied to the vector of flux C, to be defined in section 5.

Hence, we have two collocation point options and two normalized weight functions to be considered by the Chebyshev and the Legendre methods, namely: Chebyshev-Gauss-Radau, Chebyshev-Gauss-Lobatto, Legendre-Gauss-Radau and Legendre-Gauss-Lobatto.

3. Favre Average

The Navier-Stokes equations and the equations for energy and species continuity which governs the flows with multiple species undergoing chemical reactions have been used [31-33] for the analysis. Details of the present implementation for the chemical model, and the specification of the thermodynamic and transport properties are described in [34-37]. Density-weighted averaging [38] is used to derive the turbulent flow equations from the above relations. For a detailed description of the Favre equations, the g's equations and the modeling are presented in [39-40]. The interested reader is encouraged to read these papers.

4. Favre-Averaged Navier-Stokes Equations

The flow is modeled by the Favre-averaged Navier-Stokes equations in the condition of chemical non-equilibrium. Details of the five species model implementation are described in [34-37], and the interested reader is encouraged to read these works to become aware of the present study.

The reactive Navier-Stokes equations in chemical non-equilibrium were implemented on conservative and finite volume formulations, in the two-dimensional space. In this case, these equations in integral and conservative forms can be expressed by:

$$\frac{\partial}{\partial t}\int_V Q dV + \int_S \vec{F}\bullet\vec{n}dS = \int_V S_C dV + \int_V G dV \text{, with } \vec{F} = (E_e - E_v)\vec{i} + (F_e - F_v)\vec{j}, \quad (11)$$

where: Q is the vector of conserved variables, V is the volume of a computational cell, $\vec{F}$ is the complete flux vector, $\vec{n}$ is the unity vector normal to the flux face, S is the flux area, G is the k-ω two-equation model source term, S_C is the chemical source term, E_e and F_e are the convective flux vectors or the Euler flux vectors in the x and y directions, respectively, E_v and F_v are the viscous flux vectors in the x and y directions, respectively. The $\vec{i}$ and $\vec{j}$ unity vectors define the Cartesian coordinate system. Twelve (12) conservation equations are solved: one of general mass conservation, two of linear momentum conservation, one of total energy, four of species mass conservation, two of the k-ω turbulence model, and two of the g-equations. Therefore, one of the species is absent of the iterative process. The CFD literature recommends that the species of biggest mass fraction of the gaseous mixture should be omitted, aiming to result in a minor numerical accumulation error, corresponding to the biggest mixture constituent (in the case, the air). To the present study, in which is chosen a chemical model to the air composed of five (5) chemical species (N, O, N_2, O_2, and NO) and seventeen (17) chemical reactions, being fifteen (15) dissociation reactions (endothermic reactions) and two (2) of exchange or recombination, this species can be the N_2 or the O_2. To this work, the N_2 was chosen. The vectors Q, E_e, F_e, E_v, F_v, S_C and G can, hence, be defined as follows:

$$Q = \begin{Bmatrix} \rho \\ \rho u \\ \rho v \\ e \\ \rho_1 \\ \rho_2 \\ \rho_4 \\ \rho_5 \\ \rho k \\ \rho\omega \\ \rho Q_h \\ \rho Q_s \end{Bmatrix}, E_e = \begin{Bmatrix} \rho u \\ \rho u^2 + p \\ \rho uv \\ \rho Hu \\ \rho_1 u \\ \rho_2 u \\ \rho_4 u \\ \rho_5 u \\ \rho k u \\ \rho\omega u \\ \rho Q_h u \\ \rho Q_s u \end{Bmatrix}, F_e = \begin{Bmatrix} \rho v \\ \rho vu \\ \rho v^2 + p \\ \rho Hv \\ \rho_1 v \\ \rho_2 v \\ \rho_4 v \\ \rho_5 v \\ \rho k v \\ \rho\omega v \\ \rho Q_h v \\ \rho Q_s v \end{Bmatrix}, E_v = \frac{1}{Re}\begin{Bmatrix} 0 \\ t_{xx} + \tau_{xx} \\ t_{xy} + \tau_{xy} \\ f_x - \phi_x \\ -\rho_1 v_{1x} - \theta_{1x} \\ -\rho_2 v_{2x} - \theta_{2x} \\ -\rho_4 v_{4x} - \theta_{4x} \\ -\rho_5 v_{5x} - \theta_{5x} \\ \alpha_x \\ \beta_x \\ \gamma_x \\ \delta_x \end{Bmatrix}, F_v = \frac{1}{Re}\begin{Bmatrix} 0 \\ t_{xy} + \tau_{xy} \\ t_{yy} + \tau_{yy} \\ f_y - \phi_y \\ -\rho_1 v_{1y} - \theta_{1y} \\ -\rho_2 v_{2y} - \theta_{2y} \\ -\rho_4 v_{4y} - \theta_{4y} \\ -\rho_5 v_{5y} - \theta_{5y} \\ \alpha_y \\ \beta_y \\ \gamma_y \\ \delta_y \end{Bmatrix}, \quad (12)$$

in which: ρ is the mixture density; u and v are Cartesian components of the velocity vector in the x and y directions, respectively; p is the fluid static pressure; e is the fluid total energy; ρ_1, ρ_2, ρ_4 and ρ_5 are densities of the N, O, O_2 and NO, respectively; k is the turbulent kinetic energy; ω is the turbulent vorticity; Q_h is the product of fluctuating enthalpy, $\overline{h''h''}$;Q_s is the sum of the product of fluctuating mass fraction, $\sum_{i=1}^{ns} \overline{c_i'' c_i''}$; H is the mixture total enthalpy; the τ's are the components of the Reynolds stress tensor; the t's are the components of the viscous stress tensor; f_x and f_y are viscous work and Fourier heat flux functions; $\rho_s v_{sx}$ and $\rho_s v_{sy}$ represent the species diffusion flux, defined by the Fick law; ϕ_x and ϕ_y are the terms of mixture diffusion; α_x, α_y, β_x, β_y, γ_x, γ_y, δ_x and δ_y are two-equation turbulence model parameters; θ_{sx} and θ_{sy} are diffusion terms function of the mass fraction gradients; $\dot{\omega}_s$ is the chemical source term of each species equation, defined by the law of mass action; G_k and G_ω are k-ω source terms; μ_M is the molecular viscosity; μ_T is the turbulent viscosity or vorticity viscosity; Prd_L is the laminar Prandtl number; Prd_T is the turbulent Prandtl number; Sc is the laminar Schmidt number with value 0.22; Sc_T is the turbulent Schmidt number with value 1.0; h is the static enthalpy; Re is the laminar Reynolds number; and c_T is the total mass fraction sum.

$$S_C = \{0 \quad 0 \quad 0 \quad 0 \quad \dot{\omega}_1 \quad \dot{\omega}_2 \quad \dot{\omega}_4 \quad \dot{\omega}_5 \quad 0 \quad 0 \quad 0 \quad 0\}^T; \tag{13}$$

$$G = \int \begin{Bmatrix} 0 \\ 0 \\ 0 \\ 0 \\ 0 \\ 0 \\ 0 \\ 0 \\ 0 \\ G_k \\ G_\omega \\ \left(\frac{2\mu_T}{\mathrm{Re}\,\mathrm{Pr}\,d_T}\right)\left[\left(\frac{\partial h}{\partial x}\right)^2+\left(\frac{\partial h}{\partial y}\right)^2+\left(\frac{\partial h}{\partial z}\right)^2\right] \\ \left(\frac{2\mu_T}{\mathrm{Re}\,Sc_T}\right)\left[\left(\frac{\partial c_T}{\partial x}\right)^2+\left(\frac{\partial c_T}{\partial y}\right)^2+\left(\frac{\partial c_T}{\partial z}\right)^2\right]+\frac{\Psi}{\mathrm{Re}} \end{Bmatrix}. \tag{14}$$

The viscous stresses, in N/m^2, are determined, according to a Newtonian fluid model, by:

$$\begin{aligned} t_{xx} &= [2\mu_M\,\partial u/\partial x - 2/3\mu_M(\partial u/\partial x + \partial v/\partial y)]; \\ t_{xy} &= \mu_M(\partial u/\partial y + \partial v/\partial x); \\ t_{yy} &= [2\mu_M\,\partial v/\partial y - 2/3\mu_M(\partial u/\partial x + \partial v/\partial y)], \end{aligned} \tag{15}$$

The components of the turbulent stress tensor (Reynolds stress tensor) are described by the following expressions:

$$\begin{aligned} \tau_{xx} &= [2\mu_T\,\partial u/\partial x - 2/3\mu_T(\partial u/\partial x + \partial v/\partial y)] - 2/3\mathrm{Re}\rho k; \\ \tau_{xy} &= \mu_T(\partial u/\partial y + \partial v/\partial x); \\ \tau_{yy} &= [2\mu_T\,\partial v/\partial y - 2/3\mu_T(\partial u/\partial x + \partial v/\partial y)] - 2/3\mathrm{Re}\rho k. \end{aligned} \tag{16}$$

Expressions to f_x and f_y are given below:

$$f_x = (t_{xx} + \tau_{xx})u + (t_{xy} + \tau_{xy})v + q_x + k_x; \quad (17)$$

$$f_y = (t_{xy} + \tau_{xy})u + (t_{yy} + \tau_{yy})v + q_y + k_y; \quad (18)$$

where q_x and q_y are the Fourier heat flux components and are given by:

$$q_x = (\mu_M / Pr d_L + \mu_T / Pr d_T)\partial h/\partial x; \quad (19)$$

$$q_y = (\mu_M / Pr d_L + \mu_T / Pr d_T)\partial h/\partial y, \quad (20)$$

The last terms in Eqs. (17)-(18) are k_x and k_y and are defined as follows:

$$k_x = \left(\mu_M + \frac{\mu_T}{\sigma_k}\right)\partial k/\partial x,\ k_y = \left(\mu_M + \frac{\mu_T}{\sigma_k}\right)\partial k/\partial y. \quad (21)$$

The diffusion terms related to the k-ω equations are defined as:

$$\alpha_x = (\mu_M + \mu_T/\sigma_k)\partial k/\partial x,\ \alpha_y = (\mu_M + \mu_T/\sigma_k)\partial k/\partial y; \quad (22)$$

$$\beta_x = (\mu_M + \mu_T/\sigma_\omega)\partial \omega/\partial x,\ \beta_y = (\mu_M + \mu_T/\sigma_\omega)\partial \omega/\partial y; \quad (23)$$

$$\gamma_x = (\mu_M / Pr d_L + \mu_T / Pr d_T)\partial Q_h/\partial x,\ \gamma_y = (\mu_M / Pr d_L + \mu_T / Pr d_T)\partial Q_h/\partial y; \quad (24)$$

$$\delta_x = (\mu_M / Sc + \mu_T / Sc_T)\partial Q_S/\partial x,\ \delta_y = (\mu_M / Sc + \mu_T / Sc_T)\partial Q_S/\partial y. \quad (25)$$

The terms of species diffusion, defined by the Fick law, to a condition of chemical non-equilibrium, are determined by [41]:

$$\rho_s v_{sx} = -\rho D_s \frac{\partial c_s}{\partial x} \text{ and } \rho_s v_{sy} = -\rho D_s \frac{\partial c_s}{\partial y}, \quad (26)$$

with "s" referent to a given species, c_s being the mass fraction of the species, defined as:

$$c_s = \frac{\rho_s}{\rho} \quad (27)$$

and D_s is the species-effective-diffusion coefficient.

The diffusion terms ϕ_x and ϕ_y which appear in the energy equation are defined by [27]:

$$\phi_x = \sum_{s=1}^{ns} \rho_s v_{sx} h_s \text{ and } \phi_y = \sum_{s=1}^{ns} \rho_s v_{sy} h_s, \quad (28)$$

being h_s the specific enthalpy (sensible) of the chemical species "s" and "ns" is the number of species. Finally, the θ's terms of Eq. (12) are described as,

$$\theta_{sx} = (\mu_M / Sc + \mu_T / Sc_T)\partial c_S/\partial x \text{ and } \theta_{sy} = (\mu_M / Sc + \mu_T / Sc_T)\partial c_S/\partial y. \quad (29)$$

5. Numerical Scheme

Considering the two-dimensional and structured case, the algorithm follows that described in [34-37]. The speed of sound takes into account the turbulent kinetic energy by the following expression:

$$a = \sqrt{\gamma_{mixture} \frac{p}{\rho} - k}, \quad (30)$$

where $\gamma_{mixture}$ is the ratio of mixture specific heats calculated in each interaction. In other words, the mixture c_p is calculated by a weighted average involving the c_p of each species and the mass fraction of each species considered as weight; in the same form, the mixture c_v is calculated. Finally, the mixture γ is defined as the ratio of mixture c_p and mixture c_v calculated as described above.

The system is solved in two parts separately, according to [42]. The first part takes into account the dynamic part, which considers the Navier-Stokes equations plus the turbulence equations, the second one takes into

account the chemical part involving the chemical contributions. Hence, the discrete-dynamic-convective flux, which solves the dynamic and turbulent parts, is given by:

$$R_{i+1/2,j} = |S|_{i+1/2,j}\left\{\frac{1}{2}M_{i+1/2,j}\left[\begin{pmatrix}\rho a\\ \rho au\\ \rho av\\ \rho aH\\ \rho ak\\ \rho a\omega\\ \rho aQ_h\\ \rho aQ_s\end{pmatrix}_L + \begin{pmatrix}\rho a\\ \rho au\\ \rho av\\ \rho aH\\ \rho ak\\ \rho a\omega\\ \rho aQ_h\\ \rho aQ_s\end{pmatrix}_R\right] - \frac{1}{2}\phi_{i+1/2,j}\left[\begin{pmatrix}\rho a\\ \rho au\\ \rho av\\ \rho aH\\ \rho ak\\ \rho a\omega\\ \rho aQ_h\\ \rho aQ_s\end{pmatrix}_R - \begin{pmatrix}\rho a\\ \rho au\\ \rho av\\ \rho aH\\ \rho ak\\ \rho a\omega\\ \rho aQ_h\\ \rho aQ_s\end{pmatrix}_L\right]\right\} + \begin{pmatrix}0\\ S_x p\\ S_y p\\ 0\\ 0\\ 0\\ 0\\ 0\end{pmatrix}_{i+1/2,j} \tag{31}$$

and the discrete-chemical-convective flux is defined by:

$$R_{i+1/2,j} = |S|_{i+1/2,j}\left\{\frac{1}{2}M_{i+1/2,j}\left[\begin{pmatrix}\rho_1 a\\ \rho_2 a\\ \rho_4 a\\ \rho_5 a\end{pmatrix}_L + \begin{pmatrix}\rho_1 a\\ \rho_2 a\\ \rho_4 a\\ \rho_5 a\end{pmatrix}_R\right] - \frac{1}{2}\phi_{i+1/2,j}\left[\begin{pmatrix}\rho_1 a\\ \rho_2 a\\ \rho_4 a\\ \rho_5 a\end{pmatrix}_R - \begin{pmatrix}\rho_1 a\\ \rho_2 a\\ \rho_4 a\\ \rho_5 a\end{pmatrix}_L\right]\right\}, \tag{32}$$

The same definitions presented in [34-37] are valid to this algorithm. The S_x and S_y terms are normal area components, defined in Tab. 1. For better comprehension, Fig. 1 exhibits the computational cell adopted for the simulations, as well its respective nodes and flux interfaces. C can be defined as the sum of the fluxes at each interface.

The definition of the dissipation term ϕ determines the particular formulation of the convective fluxes. The choice below corresponds to the [24] scheme, according to [43]:

$$\phi_{i+1/2,j} = \phi^{VL}_{i+1/2,j} = \begin{cases} |M_{i+1/2,j}|, & \text{if } |M_{i+1/2,j}| \geq 1; \\ |M_{i+1/2,j}| + 0.5(M_R - 1)^2, & \text{if } 0 \leq M_{i+1/2,j} < 1; \\ |M_{i+1/2,j}| + 0.5(M_L + 1)^2, & \text{if } -1 < M_{i+1/2,j} \leq 0. \end{cases} \tag{33}$$

This scheme is first-order accurate in space and in time. The high-order spatial accuracy is obtained, in the current study, by the spectral method described in Section 2.

The viscous formulation follows that of [44], which adopts the Green theorem to calculate primitive variable gradients. The viscous gradients at the flux interfaces are obtained by arithmetical average between cell (i,j) and its neighbors. As was done with the convective terms, there is a need to separate the viscous flux in two parts: dynamic viscous flux, and chemical viscous flux. The dynamic part corresponds to the first four equations of the Navier-Stokes ones plus the four equations of the turbulence model, and the chemical part corresponds to the four equations immediately below the energy equation.

The Euler backward method is used to perform time integration. This method is first-order accurate in time, to the two types of complete flux. To the convective dynamic component, this method can be represented in general form by:

$$Q^{(n+1)}_{i,j} = Q^{(n)}_{i,j} - (\Delta t_{i,j}/V_{i,j}) \times [C(Q^{(n)}_{i,j})], \tag{34}$$

and to the convective chemical component, it can be represented in general form by:

$$Q^{(n+1)}_{i,j} = Q^{(n)}_{i,j} - \Delta t_{i,j} \times \{C(Q^{(n)}_{i,j})/V_{i,j} - S_C(Q^{(n)}_{i,j})\}, \tag{35}$$

where the chemical source term S_C is calculated with the translational/rotational temperature (one temperature model).

6. Turbulence Models

Five turbulence models were implemented according to a k-ω and $k^{1/2}$-ω formulations. Two turbulence models due to Coakley were implemented.

6.1. Coakley Turbulence Model – 1983

The [19] model is a $k^{1/2}$-ω one. The turbulent Reynolds number is defined as

$$R = \sqrt{k}N/\nu_M , \tag{36}$$

where: N is the normal distance from the wall to the cell under study and ν_M is the cinematic viscosity. The production term of turbulent kinetic energy is given by

$$P = \left[\left(\frac{\partial u}{\partial y}+\frac{\partial v}{\partial x}\right)\frac{\partial u}{\partial y}\right]\Big/ Re . \tag{37}$$

The function χ is defined as

$$\chi = \sqrt{C_\mu P/\omega^2} - 1 . \tag{38}$$

The damping function is given by

$$D = \frac{1-e^{-\alpha R}}{1+\beta\chi} . \tag{39}$$

The turbulent viscosity is defined by

$$\mu_T = Re\, C_\mu D\rho k/\omega , \tag{40}$$

with: C_μ a constant to be defined. According to the [19] model, the G_k and G_ω terms have the following expressions:

$$G_k = P_k + D_k \text{ and } G_\omega = P_\omega + D_\omega , \tag{41}$$

where:

$$P_k = \left(\frac{0.5C_\mu DP}{\omega^2}\right)\rho\omega\sqrt{k}/Re ;\ D_k = 0.5\left[-\frac{2}{3}\left(\frac{\partial u}{\partial x}+\frac{\partial v}{\partial y}\right)\Big/\omega - 1\right]\rho\omega\sqrt{k}/Re ; \tag{42}$$

$$P_\omega = \left(C_1 C_\mu P/\omega^2\right)\rho\omega^2/Re ;\ D_\omega = \left[-\frac{2}{3}C_1\left(\frac{\partial u}{\partial x}+\frac{\partial v}{\partial y}\right)\Big/\omega - C_2\right]\rho\omega^2/Re , \tag{43}$$

where $C_1 = 0.405D + 0.045$. The closure coefficients adopted by the [19] model are: $\sigma_k = 1.0, \sigma_\omega = 1.3$, $C_\mu = 0.09, C_2 = 0.92, \beta = 0.5, \alpha = 0.0065$, Prd_L = 0.72 and Prd_T = 0.9.

6.2. Wilcox Turbulence Model

The turbulent viscosity is expressed in terms of k and ω as:

$$\mu_T = Re\,\rho k/\omega . \tag{44}$$

In this model, the quantities σ_k and σ_ω have the values $1/\sigma^*$ and $1/\sigma$, respectively, where σ^* and σ are model constants. According to the [20] model, the G_k and G_ω terms have the following expressions:

$$G_k = P_k - D_k \text{ and } G_\omega = P_\omega - D_\omega , \tag{45}$$

where:

$$P_k = \mu_T\left[\left(\frac{\partial u}{\partial y}+\frac{\partial v}{\partial x}\right)\frac{\partial u}{\partial y}\right]\Big/ Re ;\ D_k = \beta^*\rho k\,\omega/Re ; \tag{46}$$

$$P_\omega = \left(\frac{\alpha\omega}{k}\right)P_k ; D_\omega = \beta\rho\omega^2/\mathrm{Re}, \quad (47)$$

where the closure coefficients adopted for the [20] model are: $\beta^* = 0.09, \beta = 3/40, \sigma^* = 0.5, \sigma = 0.5,$ $\alpha = 5/9$, $\mathrm{Prd_L} = 0.72$ and $\mathrm{Prd_T} = 0.9$.

6.3. Yoder, Georgiadids and Orkwis Turbulence Model

According to the [21] model, the turbulent Reynolds number is specified by:

$$\mathrm{Re_T} = \rho k/(\mu_m \omega). \quad (48)$$

The parameter α* is given by:

$$\alpha^* = (\alpha_0^* + \mathrm{Re_T}/R_k)/(1+\mathrm{Re_T}/R_k). \quad (49)$$

The turbulent viscosity is specified by:

$$\mu_T = \mathrm{Re}\,\alpha^*\rho k/\omega. \quad (50)$$

The source term denoted by G in the governing equations contains the production and dissipation terms of k and ω. To the [21] model, the G_k and G_ω terms have the following expressions:

$$G_k = P_k - D_k \text{ and } G_\omega = P_\omega - D_\omega. \quad (51)$$

To define the production and dissipation terms, it is necessary firstly to define some parameters. The turbulent Mach number is defined as:

$$M_T = \sqrt{2k/a^2}. \quad (52)$$

It is also necessary to specify the function F:

$$F = MAX(M_T^2 - M_{T,0}^2, 0.0). \quad (53)$$

The β^* parameter is given by:

$$\beta^* = 0.09\left[5/18 + (\mathrm{Re_T}/R_S)^4\right]/\left[1+(\mathrm{Re_T}/R_S)^4\right]. \quad (54)$$

Finally, the production and dissipation terms of Eq. (51) are given by

$$P_k = \tau_{xy}\frac{\partial u}{\partial y} \text{ and } D_k = \beta^*\rho\omega k(1+\xi_k F)/\mathrm{Re}; \quad (55)$$

$$P_\omega = \alpha\omega/kP_k \text{ and } D_\omega = \rho\omega^2(\beta+\beta^*\xi_\omega F)/\mathrm{Re}, \quad (56)$$

with:

$$\alpha = 5/9(\alpha_0 + \mathrm{Re_T}/R_\omega)(1+\mathrm{Re_T}/R_\omega)/\alpha^*. \quad (57)$$

The [21] turbulence model adopts the following closure coefficients: $R_s = 8.0$, $R_k = 6.0$, $R_\omega = 2.7$, $\xi_k = 1.0$, $\xi_\omega = 0.0$, $\beta = 3/40$, $M_{T,0} = 0.0$, $\alpha_0 = 0.1$, $\alpha_0^* = \beta/3$, $\sigma_k = 2.0$ and $\sigma_\omega = 2.0$.

6.4. Coakley Turbulence Model - 1997

In the [22] turbulence model, the turbulent viscosity is expressed in terms of k and ω as:

$$\mu_T = \mathrm{Re}\,C_\mu\rho k/\omega. \quad (58)$$

In this model, the quantities σ_k and σ_ω have the values $1/\sigma^*$ and $1/\sigma$, respectively, where σ^* and σ are model constants.

The source term denoted by G in the governing equations contains the production and dissipation terms of k and ω. To the [22] model, the G_k and G_ω terms have the following expressions:

$$G_k = P_k + D_k \text{ and } G_\omega = P_\omega + D_\omega. \quad (59)$$

To define the production and dissipation terms, it is necessary to define firstly some parameters. The $S_{i,j}$ gradient is defined as

$$S_{ij} = 0.5\left(\frac{\partial u}{\partial y} + \frac{\partial v}{\partial x}\right). \quad (60)$$

The gradient S is expressed as

$$S = \sqrt{2S_{ij}S_{ij}}\ . \quad (61)$$

The η parameter is defined as

$$\eta = S/\omega. \quad (62)$$

The divergent and the parameter λ are determined by

$$D = \frac{\partial u}{\partial x} + \frac{\partial v}{\partial y} \text{ and } \lambda = \frac{D}{\omega}. \quad (63)$$

The coefficients α_k and α_ω are defined by

$$\alpha_k = \frac{2}{3}\left(1 + C_\mu \lambda\right) \text{ and } \alpha_\omega = \alpha_k. \quad (64)$$

The terms of production and destruction of kinetic energy are defined as

$$P_k = C_\mu \eta^2 \rho\omega k/Re \text{ and } D_k = -\left(\alpha_k \lambda + 1\right)\rho\omega k/Re. \quad (65)$$

In relation to the terms of production and destruction of vorticity, new terms are defined. The characteristic turbulent length is expressed as

$$l = \sqrt{k}/\omega. \quad (66)$$

The coefficients $\theta_{k\omega}$ and θ_ω are defined as

$$\theta_{k\omega} = l^2\left(\frac{\partial k}{\partial x}\frac{\partial \omega}{\partial x} + \frac{\partial k}{\partial y}\frac{\partial \omega}{\partial y}\right)\Big/\left(k\omega\right) \quad (67)$$

$$\theta_\omega = l^2\left(\frac{\partial \omega}{\partial x}\frac{\partial \omega}{\partial x} + \frac{\partial \omega}{\partial y}\frac{\partial \omega}{\partial y}\right)^2\Big/\omega^2. \quad (68)$$

The turbulent Reynolds number is determined by

$$R_T = \frac{k}{\nu_m \omega}. \quad (69)$$

Some others parameters are given by

$$R = C_\mu\, R_T/R_o,\ D_v = TANH(R),\ \theta = \frac{\theta_{k\omega} - \theta_\omega}{D_v}; \quad (70)$$

$$\Delta\theta = TANH\left(|\theta| - \theta\right),\ f_{ii} = \frac{1}{\rho\sqrt{k}\omega}\left(dp/dx\right),\ f_i = f_{ii}^2; \quad (71)$$

$$\Delta f_i = TANH\left(\alpha f_i\right),\ \Delta w = 1 - \Delta\theta\left(1 - D_v^4\right); \quad (72)$$

$$C_1 = 0.675\left(1 - \Delta w\right) + \left(0.35 + 0.25\Delta f_i\right)\Delta w; \quad (73)$$

$$\sigma_w = \left(C_2 - C_1\right)\sqrt{C_\mu}\Big/\kappa^2,\ dw = 2\sigma_w \Delta w C_\mu \theta_{k\omega}. \quad (74)$$

Finally, the production and destruction terms of vorticity are defined as

$$P_\omega = C_1 C_\mu \eta^2 \rho\omega^2/Re \text{ and } D_\omega = \left(-C_1\alpha_\omega\lambda - C_2 + dw\right)\rho\omega^2/Re. \quad (75)$$

The closure coefficients assume the following values: $C_\mu = 0.09$, $C_2 = 0.833$, $\alpha = 5.0$, $\sigma_k = 1.0$, $\sigma = 0.5$, $\sigma^* = 0.5$, $\kappa = 0.41$, $R_o = 10.0$, $Prd_L = 0.72$ and $Prd_T = 0.9$.

6.5. Rumsey, Gatski, Ying and Bertelrud Turbulence Model

Finally, the k-ω model detailed in [23] has been tested. The equilibrium eddy-viscosity term employed in the diffusion terms is given by

$$\mu_T^* = \mathrm{Re}\, c_\mu^* \rho k / \omega, \tag{76}$$

where $c_\mu^* = 0.081.$ The explicit nonlinear constitutive equation that is used to close the Reynolds-averaged Navier-Stokes equations is expressed (after regularization) by

$$\rho\tau_{ii} = 2\mu_T\left[S_{ii} - \frac{1}{3}\left(S_{ii} + S_{jj}\right)\right] + \frac{2\mu_T^{'}\alpha_3}{\omega}\left(S_{ii}W_{ij} + S_{ij}W_{jj} + S_{ij}W_{ii} - S_{jj}W_{ij}\right) - \frac{4\mu_T^{'}\alpha_2}{\omega}\left(S_{ij}S_{ii} + S_{ij}S_{jj} - \frac{1}{3}S_{ij}S_{ij}\right) - \frac{2}{3}\rho k/\mathrm{Re}, \tag{77}$$

and

$$\rho\tau_{ij} = 2\mu_T S_{ij} + \frac{2\mu_T^{'}\alpha_3}{\omega}\left(S_{ii}W_{ij} + S_{ij}W_{jj} + S_{ij}W_{ii} - S_{jj}W_{ij}\right) - \frac{4\mu_T^{'}\alpha_2}{\omega}\left(S_{ij}S_{ii} + S_{ij}S_{jj}\right), \tag{78}$$

where

$$S_{ij} = \frac{1}{2}\left(\frac{\partial u_i}{\partial x_j} + \frac{\partial u_j}{\partial x_i}\right) \text{ and } W_{ij} = \frac{1}{2}\left(\frac{\partial u_i}{\partial x_j} - \frac{\partial u_j}{\partial x_i}\right) \tag{79}$$

are the mean-rate-of-strain tensor and the mean-vorticity tensor, respectively. The turbulent viscosity μ_T is

$$\mu_T = \mathrm{Re}\, c_\mu \rho k / \omega. \tag{80}$$

and

$$c_\mu = \frac{3(1+\eta^2) + 0.2(\eta^6 + \zeta^6)}{3 + \eta^2 + 6\eta^2\zeta^2 + 6\zeta^2 + \eta^6 + \zeta^6}\alpha_1; \tag{81}$$

$$\eta = (\alpha_2/\omega)(S_{ij}S_{ij})^{\frac{1}{2}} \text{ and } \zeta = (\alpha_3/\omega)(W_{ij}W_{ij})^{\frac{1}{2}}, \tag{82}$$

where:

$\alpha_1 = (4/3\text{-}C_2)(g/2)$; $\alpha_2 = (2\text{-}C_3)(g/2)$; $\alpha_3 = (2\text{-}C_4)(g/2)$; (83)

$g = (C_1/2+C_5\text{-}1)^{-1}$. (84)

The constants that govern the pressure-strain correlation model of [23] are $C_1 = 6.8$, $C_2 = 0.36$, $C_3 = 1.25$, $C_4 = 0.4$ and $C_5 = 1.88$. The $\mu_T^{'}$ terms considered in Eqs. (77-78) are given by

$$\mu_T^{'} = \mathrm{Re}\, c_\mu^{'} \rho k / \omega, \tag{85}$$

where

$$c_\mu^{'} = \frac{3(1+\eta^2)}{3 + \eta^2 + 6\eta^2\zeta^2 + 6\zeta^2 + \eta^6 + \zeta^6}\alpha_1. \tag{86}$$

The source term denoted by G in the governing equation contains the production and dissipation terms of k and ω. To the [23] model, the G_k and G_ω terms have the following expressions:

$$G_k = P_k - D_k \text{ and } G_\omega = P_\omega - D_\omega, \tag{87}$$

where:

$$P_k = \rho\left(\tau_{xy}\frac{\partial u}{\partial y}\right),\ D_k = \rho\omega k/\mathrm{Re}; \tag{88}$$

$$P_\omega = \psi\rho\omega\left(\tau_{xy}\frac{\partial u}{\partial y}\right)\Big/ k, \text{ and } D_\omega = \beta\rho\omega^2/Re. \quad (89)$$

The closure coefficients adopted to the [23] model assume the following values: $\beta = 0.83, \kappa = 0.41$, $\sigma_k = 1.4, \sigma_\omega = 2.2$, $Prd_L = 0.72$, $Prd_T = 0.9$ and $\psi = \beta - \left[\kappa^2/\sigma_\omega\sqrt{c_\mu^*}\right]$.

7. Spatially Variable Time Step

The spatially variable time step has proved efficient gains in terms of convergence acceleration, as proved by [25-26].The total pressure of the gaseous mixture is determined by Dalton law, which indicates that the total pressure of the gas is the sum of the partial pressure of each constituent gas, resulting in:

$$p_s = c_s\rho R_s T \text{ and } p = \sum_{s=1}^{ns} p_s. \quad (90)$$

The speed of sound to a reactive mixture and considering turbulence modeling can be, hence, determined by Eq. (30). Finally, the spatially variable time step is defined from the CFL (Courant-Friedrichs-Lewis) definition:

$$\Delta t_{i,j} = \frac{CFL\Delta s_{i,j}}{\sqrt{u_{i,j}^2 + v_{i,j}^2} + a_{i,j}}, \quad (91)$$

where $\Delta s_{i,j}$ is the characteristic length of each cell (defined between the minimum cell side length and the minimum centroid distance between each cell and its neighbors).

8. Dimensionless, Initial and Boundary Conditions

8.1. Dimensionless

The dimensionless employed to the chemical non-equilibrium case consisted in: R_s is dimensionless by a_{char}, where $a_{char} = \sqrt{\gamma p_{char}/\rho_{char}}$; c_v is dimensionless by a_{char}; h_s and h_s^0 are dimensionless by a_{char}^2; T, translational/rotational temperature, is dimensionless by a_{char}; ρ_s and ρ are dimensionless by ρ_{char}; u and v are dimensionless by a_{char}; μ is dimensionless by μ_{char}; D, diffusion coefficient, dimensionless by $a_{char}^2\, dt_{char}$, where dt_{char} is the minimum time step calculated in the computational domain at the first iteration; $\dot{\omega}$ is dimensionless by $(\rho_{char}/dt_{char})x10^{-3}$; e and p are dimensionless by $\rho_{char}a_{char}^2$. The characteristic properties are obtained from [45].

8.2. Initial Condition

The initial conditions to the blunt body and reentry capsule problems, for a five species chemical model, are presented in Tabs. 2-3. L_{REF} is the reference length, equal to L in the present study. The Reynolds number is obtained from data provided in [45].

8.3. Boundary Conditions

The boundary conditions are basically of four types: solid wall, entrance, exit and continuity. These conditions are implemented with the help of ghost cells.

Wall condition

At a solid boundary the non-slip condition is enforced. Therefore, the tangent velocity component of the ghost volume at wall has the same magnitude as the respective velocity component of its real neighbor cell, but opposite signal. In the same way, the normal velocity component of the ghost volume at wall is equal in value, but opposite in signal, to the respective velocity component of its real neighbor cell.

The normal pressure gradient of the fluid at the wall is assumed to be equal to zero in a boundary-layer like condition. The same hypothesis is applied for the normal temperature gradient at the wall, assuming an adiabatic wall. From the above considerations, density and translational/rotational temperature are extrapolated from the respective values of its real neighbor volume (zero order extrapolation).

With the species mass fractions and with the definition of the internal energy for each gas, it is possible to obtain the mixture internal energy of the ghost volume. The mixture formation enthalpy is extrapolated from the real cell. The mixture total energy to the ghost cell is calculated by:

$$e_g = \rho_g \left[e_{i,g} + \Delta h^0_{mixture,g} + 0.5\left(u_g^2 + v_g^2\right)\right], \quad (92)$$

where "g" reports to "ghost" cell and $e_{i,g}$ is the ghost internal energy. To the species density, the non-catalytic condition is imposed, what corresponds to zero order extrapolation from the real cell species densities.

The turbulent kinetic energy and the turbulent vorticity at the ghost volumes are determined by the following expression, for all models:

$$k_{ghost} = 0.0 \text{ and } \omega_{ghost} = \left[\left(38/3\nu_M\right)/\left(\overline{\beta} d_n^2\right)\right], \quad (93)$$

where $\overline{\beta}$ assumes the value 3/40 and d_n is the distance of the first cell to the wall. Values to Q_h and Q_s at the boundary are the same as the initial condition.

Entrance condition

It is divided in two flow regimes:

(a) Subsonic flow: Seven properties are specified and one extrapolated in the boundary conditions of the dynamic part of the algorithm. This approach is based on information propagation analysis along characteristic directions in the calculation domain ([46]). In other words, for subsonic flow, seven characteristic propagate information point into the computational domain. Thus seven flow properties must be fixed at the inlet plane. Just one characteristic line allows information to travel upstream. So, one flow variable must be extrapolated from the grid interior to the inlet boundary. The total energy was the extrapolated variable from the real neighbor volumes, for the studied problems. Density and velocity components adopted values of initial flow. The turbulence kinetic energy and the vorticity are prescribed and receive the following values: $k = 0.01k_{ff}$ and $10u/L_{REF}$, respectively, where $k_{ff} = 0.5u^2$. For the [19] turbulence model, consider $k = \sqrt{0.01k_{ff}}$. Q_h and Q_s are also fixed with the values $10^{-6} h^2_{initial}$ and $10^{-3}\sum_{s=1}^{ns} c^2_{s,initial}$, respectively. To the chemical part, four information propagate upstream because it is assumed that all four equations are conducted by the eigenvalue "$(q_n$-a)". In the subsonic flow, all eigenvalues are negative and the information should be extrapolated. Hence, all of them should be extrapolated.

(b) Supersonic flow: In this case no information travels upstream; therefore all variables are fixed with their initial values.

Exit condition

It is also divided in two flow regimes:

(a) Subsonic flow: Seven characteristic propagate information outward the computational domain. Hence, the associated variables should be extrapolated from interior information. The characteristic direction associated to the "$(q_{normal}$-a)" velocity should be specified because it points inward to the computational domain [46]. In this case, the ghost volume total energy is specified from its initial value. Density, velocity components and turbulent variables are extrapolated. To the chemical part, the eigenvalue "$(q_n$-a)" is again negative and the characteristics are always flowing into the computational domain. Hence, the four chemical species under study should have their densities fixed by their initial values.

(b) Supersonic flow: All variables are extrapolated from interior grid cells, as no flow information can make its way upstream. In other words, nothing can be fixed.

Continuity condition

This condition imposes continuity of the flow at the trailing edge of the reentry capsule configuration. This is done considering the Kutta condition in this region. In terms of numerical implementation, it is obtained considering the vector of conserved variables above the wake as equal to the vector of conserved variables below the wake.

9. Physical Problems and Meshes

Two physical problems were solved in this work, namely: blunt body, and reentry capsule. The first problem considers the geometry of a blunt body with 1.0 m of nose ratio and parallel rectilinear walls. The far field is located at 20.0 times the nose ratio in relation to the configuration nose. A mesh composed of 2,548 rectangular cells and 2,650 nodes with an exponential stretching of 5.0% was studied. This mesh is equivalent in finite differences to a one of 53x50 points. Figure 2 shows the detail of the geometry and Figure 3 exhibit the viscous mesh.

The second problem is the geometry of the reentry capsule. Details of the configuration are presented in Fig. 4. The far field is located at 20.0 unities. A mesh of 3,136 rectangular cells and 3,250 nodes with an exponential stretching of 5.0% was used for the viscous simulations. This mesh is equivalent in finite differences to a one of 65x50 points. Figure 5 show this viscous mesh.

10. Results

Tests were performed in a Core i7 processor of 2.8GHz and 6.0Gbytes of RAM microcomputer, in a Windows 7.0 environment. Three (3) orders of reduction of the maximum residual in the field were considered to obtain a converged solution. The residual was defined as the value of the discretized conservation equation. In the dynamic part of the [24] scheme, such definition results in:

$$\text{Residual} = -\Delta t_{i,j} / V_{i,j} \times C_{i,j}. \quad (94)$$

The attack angle was adopted equal to zero. In this work, the blunt body turbulent results were obtained for a 4^{th} order of accuracy of the spectral method, whereas the reentry capsule turbulent solutions were obtained for an 16^{th} order of accuracy of the spectral method. For a matter of simplicity, the following abbreviations were used: [24] scheme = VL, [19] model = C83, [20] model = W88, [21] model = YGO96, [22] model = C97, [23] model = RGYB98, Chebyshev-Gauss-Radau = CGR, Chebyshev-Gauss-Lobatto = CGL, Legendre-Gauss-Radau = LGR, and Legendre-Gauss-Lobatto = LGL.

10.1. Blunt Body Problem

Figures 6 to 13 show the pressure and temperature contours obtained by the VL scheme as using the CGR, CGL, LGR, and LGL collocation points coupled with the C83 turbulence model. All solutions capture the shock wave and good symmetry properties are observed as in pressure contours as in temperature contours. The most intense pressure field when considering only the C83 model is obtained as using the CGR collocation points. The most intense temperature field considering only the C83 model is detected as using the LGR collocation points.

Figures 14 to 21 show the pressure and temperature contours obtained by the VL scheme when using the CGR, CGL, LGR, and LGL collocation points coupled with the W88 turbulence model. The maximum-pressure peak considering only W88 model is obtained when using the CGR collocation points. Good symmetry properties are observed, and the normal shock wave is well captured by the numerical scheme.

Figures 22 to 29 exhibit the pressure and temperature contours calculated with the VL scheme when using the CGR, CGL, LGR, and LGL collocation points coupled with the YGO96 turbulence model. As can be verified, good shock resolution is observed in the figures. The viscous layer is well captured in the temperature contours, highlighting the good transport of viscous properties, like viscosity and thermal conduction. Good symmetry properties are observed in all figures. Some pressure oscillations are observed in Fig. 24.

Figures 30 to 37 present the pressure and temperature contours generated by the VL scheme as using the CGR, CGL, LGR, and LGL collocation points coupled with the C97 turbulence model. Some pressure oscillations are observed in Fig. 32, but the shock wave is well captured by the numerical scheme. Good transport of viscous

properties is observed in the viscous layer, as shown in Figs. 31, 33, 35, and 37. The maximum pressure peak is obtained by the VL scheme as using the CGR collocation points.
Finally, Figs. 38 to 45 show the pressure and temperature contours obtained by the VL scheme as using the CGR, CGL, LGR and LGL collocation points coupled with RGYB98 turbulence model. Good symmetry properties are observed in all figures. No pressure oscillations are observed in these figures. Good transport of viscous properties is verified. The shock wave is well captured by the numerical scheme in its variants.

10.2. Reentry Capsule Problem

Figures 46 to 53 present the pressure and temperature contours generated by the VL scheme as using the CGR, CGL, LGR, and LGL collocation points coupled with the C83 turbulence model. The maximum-pressure peak for this turbulence model is obtained by the CGR collocation points. Good symmetry properties are observed in all figures. The shock wave is well captured by the numerical scheme.
Figures 54 to 61 exhibit the pressure and temperature contours calculated by the VL scheme when using the CGR, CGL, LGR, and LGL collocation points coupled with the W88 turbulence model. Solutions free of oscillations are verified. Good symmetry properties are verified in all figures.
Figures 62 to 69 show the pressure and temperature contours obtained by the VL scheme as using the CGR, CGL, LGR, and LGL collocation points coupled with the YGO96 turbulence model. Some oscillations are verified in Fig. 64, but the shock wave is well captured. The wake is well captured, highlighting the excellent treatment of this frontier by the boundary condition.
Figures 70 to 77 presents the pressure and temperature contours calculated by the VL scheme when using the CGR, CGL, LGR, and LGL collocation points coupled with the C97 model. Homogeneous solutions are observed in the field. The maximum-pressure peak for this turbulence model is obtained when using CGR collocation points. Good symmetry properties are again verified. The wake and the shock wave are well detected by the numerical scheme.
Figures 78 to 85 exhibit the pressure and temperature contours generated by the VL scheme as using the CGR, CGL, LGR, and LGL collocation points coupled with the RGYB98 model. The maximum-pressure peak with this turbulence model is obtained as using the CGR collocation points. Good symmetry properties are observed. As can be observed, the CGR collocation points always pointed to the maximum-pressure peak in the field in all cases studied in this work. On the other hand, the maximum temperature peak is generally obtained by the LGR collocation points.

10.3. Other Results

Figure 86 shows the convergence history of the VL schem to a 4^{th} order spectral method using LGR for collocation points and to an ENO solution also of 4^{th} order using Newton interpolation function, both coupled with the C83 turbulence model, to the blunt body viscous case. The LGR collocation points were chosen because they provide the best convergence of the VL scheme for the turbulent case coupled with the C83 model for a formal 4^{th} order of accuracy. The ENO procedure was implemented by the author and was used for numerical comparisons. To details of the implementation of the ENO procedure on a context of chemical non-equilibrium and with turbulence actuation, the reader is encouraged to read [47, 48]. As can be seen in Fig. 86, the spectral LGR method coupled with the VL scheme and the C83 turbulence model was the most efficient converging in 754 iterations, with a maximum CFL of 0.30. The ENO solution was inefficient compared with the spectral method. The maximum allowable CFL number employed in the ENO solution was 0.10, converging in 2,750 iterations.
As conclusion, the correct implementation of the proposed spectral method guide us to an efficient high order scheme, converging in less than 800 iterations in the turbulent case, for the blunt body problem, when programmed coupled with the VL scheme. The LGR variant of the spectral method for the turbulent case was the most efficient in the studies performed by the author and ratified the fast convergence as expected.

10.4. Quantitative Analysis

In order to perform a quantitative analysis, the present reactive results are compared to the perfect gas solutions.

The stagnation pressures at the blunt body nose, and at the reentry capsule nose were evaluated assuming the perfect gas formulation. Such parameter calculated at this way is not the best comparison, but in the absence of practical reactive results, this constitutes the best available solution.

To calculate the stagnation pressure at the nose of these two configurations, [49] presents in its B Appendix values of the normal shock wave properties ahead of the configuration. The ratio pr_0/pr_∞ is estimated as function of the normal Mach number and the stagnation pressure pr_0 can be determined from this parameter. Hence, Table 4 gives the theoretical stagnation pressure values obtained for the two configurations at the initial-normal-Mach number. The value of pr_∞ is determined by the following expression:

$$pr_\infty = \frac{pr_{initial}}{\rho_{char} \times a_{char}^2}, \tag{95}$$

where, for example, for the blunt body case, $pr_{initial}$ = 687N/m^2, ρ_{char} = 0.004kg/m^3 and a_{char} = 317.024m/s. Considering these values, one concludes that pr_∞ = 1.709 (non-dimensional). Using the ratio obtained from [49], the stagnation pressure ahead of the configuration nose is estimated as 170.87 unities. Table 5 compares values of the stagnation pressure obtained from the simulations with the theoretical values and show the percentage errors. As can be seen, the best result for the blunt body problem is provided by the CGL collocation points, with an error of 2.66%, when coupled with the VL scheme and the C83 turbulence model; and by the CGL collocation points again, with an error of 3.88%, when coupled with the VL scheme and the YGO96 turbulence model, for the reentry capsule problem.

As the hypersonic flows around the blunt body, and reentry capsule configurations were simulated with a zero value to the attack angle, a zero lift coefficient, due to geometry symmetry, is the expected value for this aerodynamic coefficient. Table 6 presents an analysis of the lift aerodynamic coefficient, based only on pressure contribution, in this study. As can be observed, the best value to the lift coefficient for the blunt body problem is obtained by the LGR collocation points, coupled with the VL scheme and the C83 turbulence model; and by the LGL collocation points, coupled with the VL scheme and the C83 turbulence model again, for the reentry capsule problem.

10.5 . Computational Performance

Table 7 presents the computational data of the VL scheme for the blunt body, and for the reentry capsule problems. It shows the CFL number and the number of iterations to convergence for all studied cases in the current work. It can be verified that the best performance of the VL scheme for the blunt body problem is obtained coupled with the C83 turbulence model as using the LGR collocation points, employing a CFL of 0.30, and converging in 754 iterations. On the other hand, the best performance of the VL scheme for the reentry capsule problem occurred again when using the LGR collocation points, employing a CFL of 0.30, and converging in 630 iterations, when coupled with the C83 turbulence model.

As final conclusion, it is possible to highlight that, for the blunt body problem, the VL scheme coupled with the C83 turbulence model using CGL collocation points had the best performance in estimating the stagnation pressure, and the lift aerodynamic coefficient was better estimated by the VL scheme as using the LGR collocation points also coupled with the C83 turbulence model; and for the reentry capsule problem, the VL scheme coupled with the YGO96 turbulence model using CGL collocation points had the best performance in estimating the stagnation pressure, and the lift aerodynamic coefficient was better estimated by the VL scheme as using the LGL collocation points also coupled with the C83 turbulence model. Moreover, the best performance of the numerical scheme, for the 4th order of accuracy, was coupled with the C83 turbulence model, when using the LGR collocation points, employing a CFL of 0.30, and converging in 754 iterations, whereas for the 16th order of accuracy, the best performance of the numerical scheme was coupled with the C83 turbulence model, when using the LGR collocation points, employing a CFL of 0.30, and converging in 630 iterations.

Finally, to close this work, the computational cost of the numerical scheme using the several types of collocation points is presented in Tabs. 8-9. For the 4th order of accuracy, the cheapest combination was the VL scheme coupled with W88 turbulence model and using LGL collocation points with a cost of 0.0002292 sec/per-volume/per-iteration, whereas for the 16th order of accuracy the cheapest was due to the VL scheme coupled

with the YGO96 turbulence model and using the CGR collocation points with a cost of 0.0005523 sec/per-volume/per-iteration.

Table 1: Values of S_x and S_y

Surface	S_x	S_y
i,j-1/2	$\left(y_{i+1,j} - y_{i,j}\right)$	$\left(x_{i,j} - x_{i+1,j}\right)$
i+1/2,j	$\left(y_{i+1,j+1} - y_{i+1,j}\right)$	$\left(x_{i+1,j} - x_{i+1,j+1}\right)$
i,j+1/2	$\left(y_{i,j+1} - y_{i+1,j+1}\right)$	$\left(x_{i+1,j+1} - x_{i,j+1}\right)$
i-1/2,j	$\left(y_{i,j} - y_{i,j+1}\right)$	$\left(x_{i,j+1} - x_{i,j}\right)$

Table 2: Initial conditions to the blunt body problem

Property	Value
$M_{initial}$	8.78
$\rho_{initial}$	0.00326 kg/m^3
$pr_{initial}$	687 Pa
$U_{initial}$	4,776 m/s
$T_{initial}$	694 K
Altitude	40,000 m
c_N	10^{-9}
c_O	0.07955
c_{O2}	0.13400
c_{NO}	0.05090
L_{REF}	2.0 m
Re_{char}	2.386x10^6
$k_{initial}$	10^{-6}
$\omega_{initial}$	$10U_{initial}/L_{REF}$
$Q_{h,initial}$	$10^{-4} h^2_{initial}$
$Q_{s,initial}$	$10^{-2}\sum_{i=1}^{ns} c^2_{i,initial}$

Table 3: Initial conditions to the reentry capsule problem

Property	Value
$M_{initial}$	10.6
$\rho_{initial}$	0.02863 kg/m^3
$pr_{initial}$	3,885 Pa
$U_{initial}$	4,628 m/s
$T_{initial}$	473 K
Altitude	40,000 m
c_N	10^{-9}
c_O	0.07955
c_{O2}	0.13400
c_{NO}	0.05090
L_{REF}	3.0 m
Re_{char}	3.468x10^6
$k_{initial}$	10^{-6}
$\omega_{initial}$	$10U_{initial}/L_{REF}$

$Q_{h,initial}$	$10^{-4} h^2_{initial}$
$Q_{s,initial}$	$10^{-2} \sum_{i=1}^{ns} c^2_{i,initial}$

Table 4: Values of theoretical stagnation pressure

Problem:	**$M_{initial}$:**	**pr_0/pr_∞:**	**pr_∞:**	**pr_0 (Theoretical):**
Blunt body	8.78	99.98	1.709	170.87
Reentry capsule	10.6	145.46	9.664	1,405.73

Table 5: Values of stagnation pressure and respective errors

Physical Problem:	**Turbulence Model:**	**Spectral Method:**	**pr_0: (Numerical)**	**Error:**
Blunt Body (4^{th} Order) (pr_0 = 170.87)	Coakley (1983)	CGR	186.57	9.19
		CGL	166.32	2.66
		LGR	142.97	16.33
		LGL	152.36	10.83
	Wilcox (1988)	CGR	198.05	15.91
		CGL	177.20	3.70
		LGR	143.10	16.25
		LGL	151.58	11.29
	YGO (1996)	CGR	197.97	15.86
		CGL	177.13	3.66
		LGR	143.06	16.28
		LGL	151.56	11.30
	Coakley (1997)	CGR	197.97	15.86
		CGL	177.14	3.67
		LGR	143.06	16.28
		LGL	151.56	11.30
	RGYB (1998)	CGR	197.98	15.87
		CGL	177.15	3.68
		LGR	143.06	16.28
		LGL	151.56	11.30
Reentry Capsule (16^{th} Order) (pr_0 = 1405.73)	Coakley (1983)	CGR	1,516.87	7.91
		CGL	1,463.45	4.11
		LGR	1,110.72	20.99
		LGL	1,113.53	20.79
	Wilcox (1988)	CGR	1,512.70	7.61
		CGL	1,462.22	4.02
		LGR	1,109.06	21.10
		LGL	1,111.94	20.90
	YGO (1996)	CGR	1,511.91	7.55
		CGL	1,460.23	3.88
		LGR	1,108.42	21.15
		LGL	1,111.19	20.95
	Coakley (1997)	CGR	1,512.23	7.58
		CGL	1,460.48	3.89
		LGR	1,108.51	21.14
		LGL	1,111.28	20.95
	RGYB (1998)	CGR	1,492.55	6.18
		CGL	1,461.51	3.97

	LGR	1,108.63	21.13
	LGL	1,111.55	20.93

Table 6: Values of lift aerodynamic coefficient

Physical Problem:	Turbulence Model:	Spectral Method:	c_L:
Blunt Body (4^{th} Order)	Coakley (1983)	CGR	3.4539×10^{-13}
		CGL	1.4063×10^{-13}
		LGR	3.7615×10^{-14}
		LGL	5.9045×10^{-14}
	Wilcox (1988)	CGR	1.4758×10^{-11}
		CGL	6.7084×10^{-12}
		LGR	2.0571×10^{-12}
		LGL	2.7263×10^{-12}
	YGO (1996)	CGR	4.3244×10^{-13}
		CGL	1.9694×10^{-13}
		LGR	5.6360×10^{-14}
		LGL	7.2430×10^{-14}
	Coakley (1997)	CGR	3.6155×10^{-12}
		CGL	1.2655×10^{-12}
		LGR	3.4263×10^{-13}
		LGL	4.6925×10^{-13}
	RGYB (1998)	CGR	-6.5017×10^{-06}
		CGL	-2.2084×10^{-06}
		LGR	-3.5759×10^{-06}
		LGL	-2.9655×10^{-06}
Reentry Capsule (16^{th} Order)	Coakley (1983)	CGR	-2.6933×10^{-09}
		CGL	-1.5419×10^{-08}
		LGR	3.8242×10^{-11}
		LGL	3.0848×10^{-11}
	Wilcox (1988)	CGR	2.7734×10^{-06}
		CGL	-5.9709×10^{-07}
		LGR	-5.6410×10^{-07}
		LGL	-2.8482×10^{-07}
	YGO (1996)	CGR	-1.9102×10^{-07}
		CGL	-1.7173×10^{-07}
		LGR	-7.4149×10^{-09}
		LGL	-7.4846×10^{-09}
	Coakley (1997)	CGR	-4.4359×10^{-08}
		CGL	-4.3042×10^{-08}
		LGR	-3.2714×10^{-08}
		LGL	-3.2832×10^{-08}
	RGYB (1998)	CGR	-8.3037×10^{-06}
		CGL	-5.9528×10^{-06}
		LGR	-47125×10^{-06}
		LGL	-5.0541×10^{-06}

Table 7: Computational data

Physical Problem:	Turbulence Model:	Spectral Method:	CFL:	Iterations:
	Coakley (1983)	CGR	0.70	961
		CGL	0.50	782

		LGR	0.30	754
		LGL	0.30	882
	Wilcox (1988)	CGR	0.70	1,005
		CGL	0.50	786
		LGR	0.30	773
		LGL	0.30	904
	YGO (1996)	CGR	0.70	1,004
Blunt Body (4^{th} Order)		CGL	0.50	780
		LGR	0.30	772
		LGL	0.30	903
	Coakley (1997)	CGR	0.70	995
		CGL	0.50	777
		LGR	0.30	769
		LGL	0.30	900
	RGYB (1998)	CGR	0.70	995
		CGL	0.50	777
		LGR	0.30	769
		LGL	0.30	900
	Coakley (1983)	CGR	0.50	854
		CGL	0.50	782
		LGR	0.30	630
		LGL	0.08	1,398
	Wilcox (1988)	CGR	0.10	3,371
		CGL	0.10	3,139
		LGR	0.08	1,308
		LGL	0.08	1,330
	YGO (1996)	CGR	0.10	3,345
Reentry Capsule (16^{th} Order)		CGL	0.10	3,117
		LGR	0.08	1,339
		LGL	0.08	1,329
	Coakley (1997)	CGR	0.10	3,342
		CGL	0.10	3,108
		LGR	0.08	1,338
		LGL	0.08	1,329
	RGYB (1998)	CGR	0.10	3,312
		CGL	0.10	3,104
		LGR	0.08	1,309
		LGL	0.08	1,334

Table 8: Computational cost (4^{th} Order)

Turbulence Model:	**Spectral Method:**	**Cost (sec/per-volume/per-iteration)**
Coakley (1983)	Chebyshev-Gauss-Radau	0.0003455
	Chebyshev-Gauss-Lobatto	0.0002324
	Legendre-Gauss-Radau	0.0002321
	Legendre-Gauss-Lobatto	0.0003391
Wilcox (1988)	Chebyshev-Gauss-Radau	0.0003308
	Chebyshev-Gauss-Lobatto	0.0002302
	Legendre-Gauss-Radau	0.0003412
	Legendre-Gauss-Lobatto	0.0002292

YGO (1996)	Chebyshev-Gauss-Radau	0.0003510
	Chebyshev-Gauss-Lobatto	0.0002380
	Legendre-Gauss-Radau	0.0003401
	Legendre-Gauss-Lobatto	0.0002308
Coakley (1997)	Chebyshev-Gauss-Radau	0.0003538
	Chebyshev-Gauss-Lobatto	0.0002399
	Legendre-Gauss-Radau	0.0003358
	Legendre-Gauss-Lobatto	0.0003323
RGYB (1998)	Chebyshev-Gauss-Radau	0.0002339
	Chebyshev-Gauss-Lobatto	0.0003425
	Legendre-Gauss-Radau	0.0003430
	Legendre-Gauss-Lobatto	0.0003423

Table 9: Computational cost (16th Order)

Turbulence Model:	**Spectral Method:**	**Cost (sec/per-volume/per-iteration)**
Coakley (1983)	Chebyshev-Gauss-Radau	0.0005663
	Chebyshev-Gauss-Lobatto	0.0005816
	Legendre-Gauss-Radau	0.0005823
	Legendre-Gauss-Lobatto	0.0005593
Wilcox (1988)	Chebyshev-Gauss-Radau	0.0005798
	Chebyshev-Gauss-Lobatto	0.0005598
	Legendre-Gauss-Radau	0.0005573
	Legendre-Gauss-Lobatto	0.0005778
YGO (1996)	Chebyshev-Gauss-Radau	0.0005523
	Chebyshev-Gauss-Lobatto	0.0005779
	Legendre-Gauss-Radau	0.0005604
	Legendre-Gauss-Lobatto	0.0005931
Coakley (1997)	Chebyshev-Gauss-Radau	0.0005633
	Chebyshev-Gauss-Lobatto	0.0005627
	Legendre-Gauss-Radau	0.0005596
	Legendre-Gauss-Lobatto	0.0005607
RGYB (1998)	Chebyshev-Gauss-Radau	0.0005676
	Chebyshev-Gauss-Lobatto	0.0006452
	Legendre-Gauss-Radau	0.0005790
	Legendre-Gauss-Lobatto	0.0005610

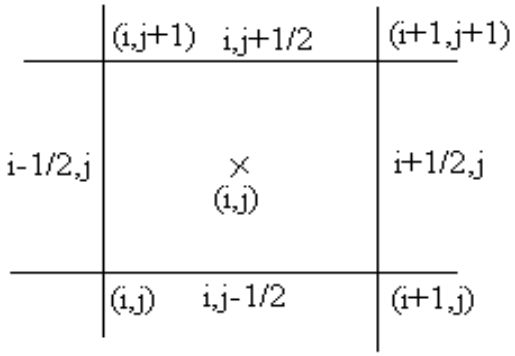

Figure 1: Computational cell

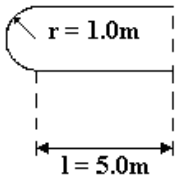

Figure 2. Blunt body geometry

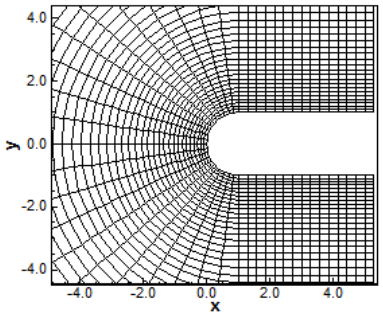

Figure 3. Blunt body viscous mesh

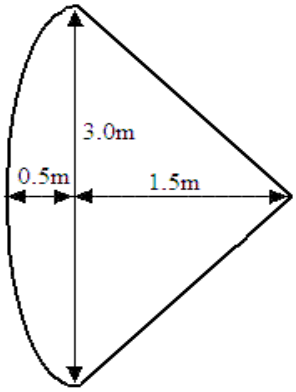

Figure 4: Reentry capsule geometry

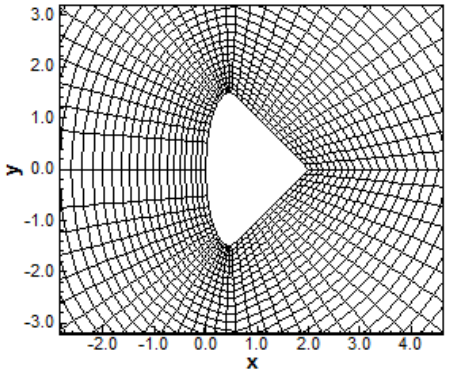

Figure 5: Reentry capsule viscous mesh

BLUNT BODY TURBULENT SOLUTIONS – 4th ORDER

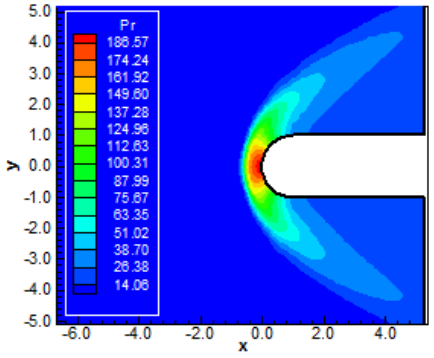

Figure 6: Pressure contours (CGR-C83)

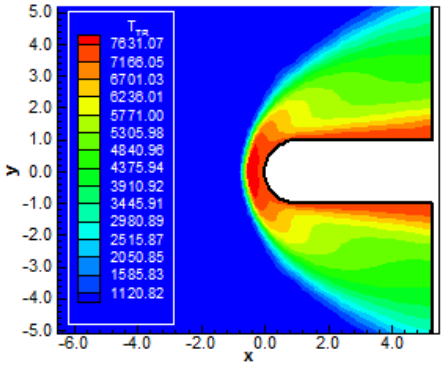

Figure 7: Temperature contours (CGR-C83)

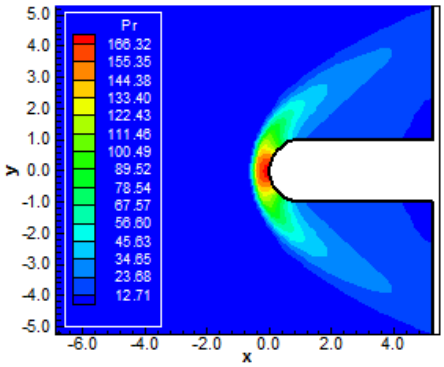

Figure 8: Pressure contours (CGL-C83)

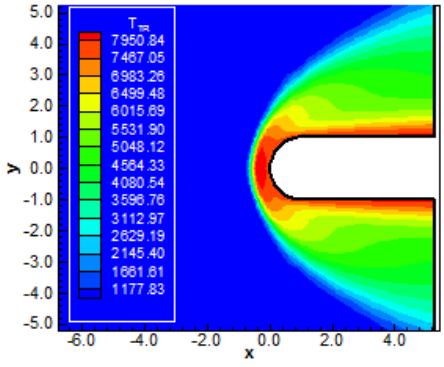

Figure 9: Temperature contours (CGL-C83)

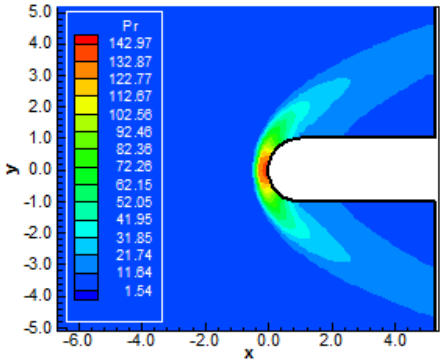

Figure 10: Pressure contours (LGR-C83)

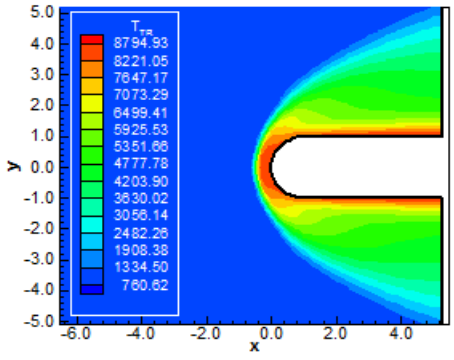

Figure 11: Temperature contours (LGR-C83)

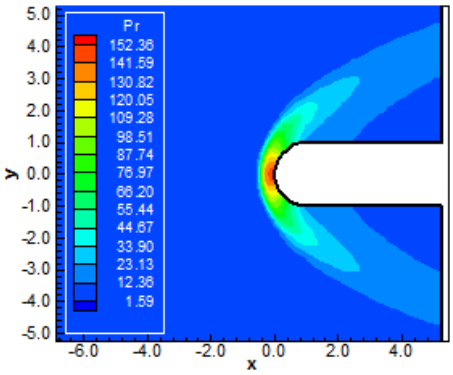

Figure 12: Pressure contours (LGL-C83)

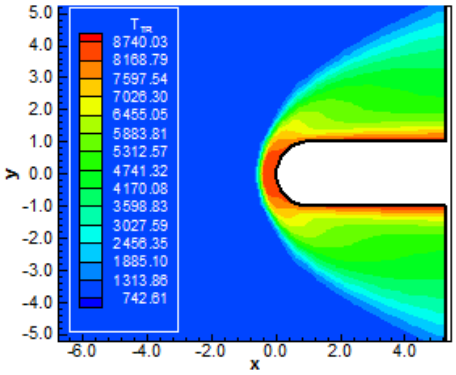

Figure 13: Temperature contours (LGL-C83)

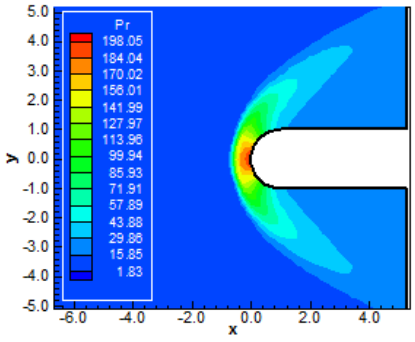

Figure 14: Pressure contours (CGR-W88)

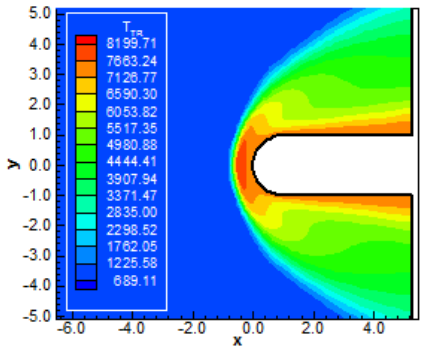

Figure 15: Temperature contours (CGR-W88)

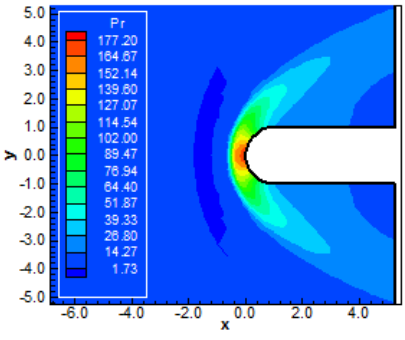

Figure 16: Pressure contours (CGL-W88)

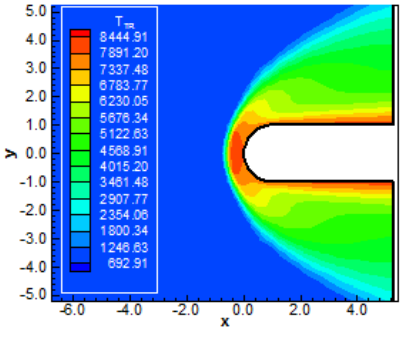

Figure 17: Temperature contours (CGL-W88)

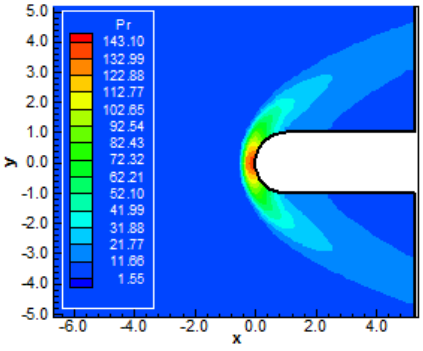

Figure 18: Pressure contours (LGR-W88)

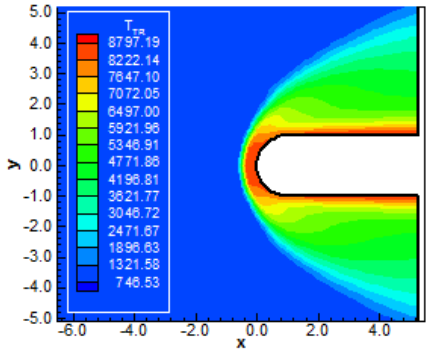

Figure 19: Temperature contours (LGR-W88)

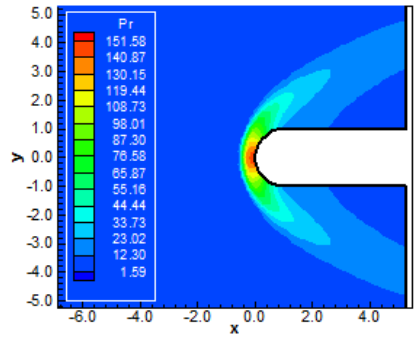

Figure 20: Pressure contours (LGL-W88)

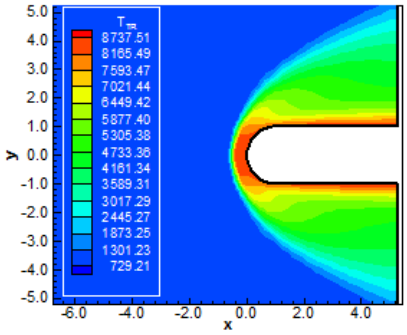

Figure 21: Temperature contours (LGL-W88)

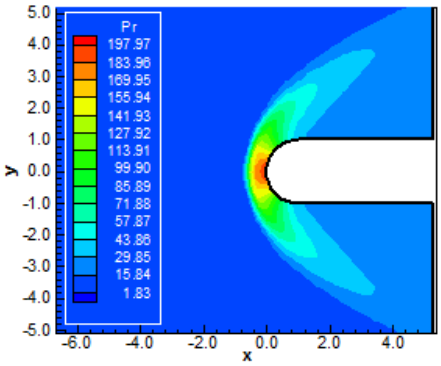

Figure 22: Pressure contours (CGR-YGO96)

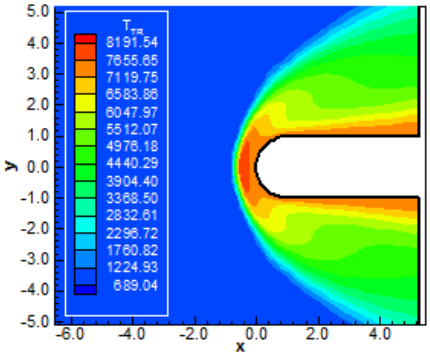

Figure 23: Temperature contours (CGR-YGO96)

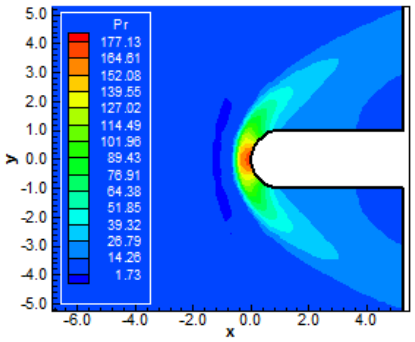

Figure 24: Pressure contours (CGL-YGO96)

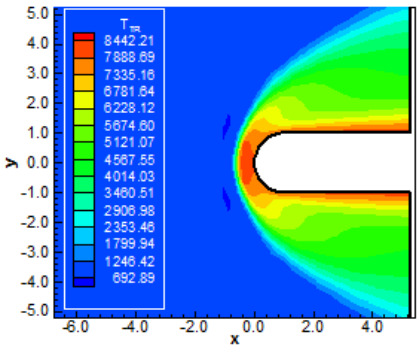

Figure 25: Temperature contours (CGL-YGO96)

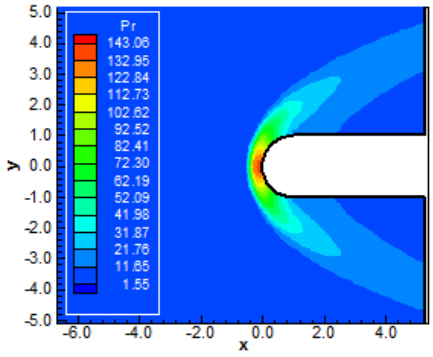

Figure 26: Pressure contours (LGR-YGO96)

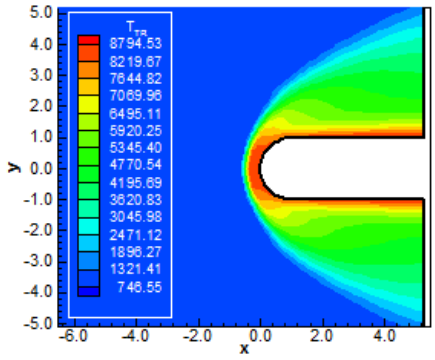

Figure 27: Temperature contours (LGR-YGO96)

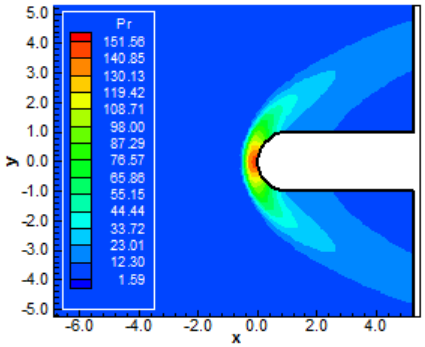

Figure 28: Pressure contours (LGL-YGO96)

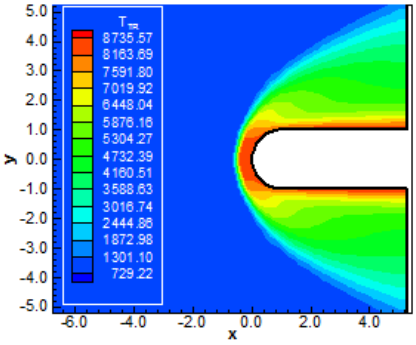

Figure 29: Temperature contours (LGL-YGO96)

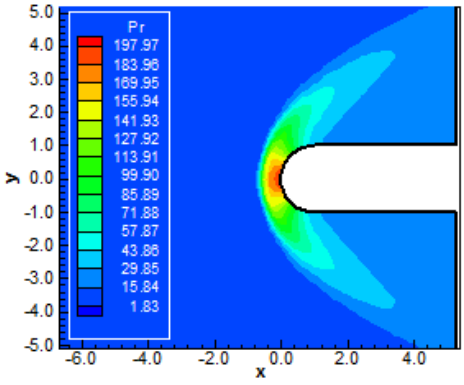

Figure 30: Pressure contours (CGR-C97)

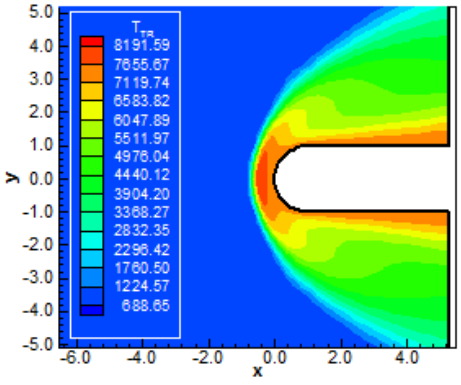

Figure 31: Temperature contours (CGR-C97)

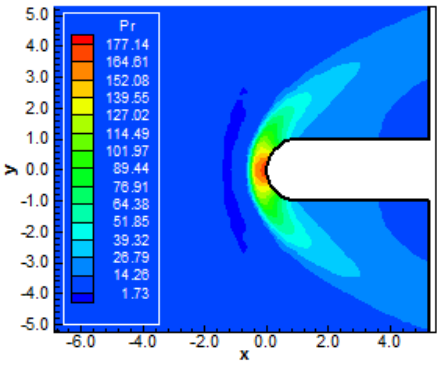

Figure 32: Pressure contours (CGL-C97)

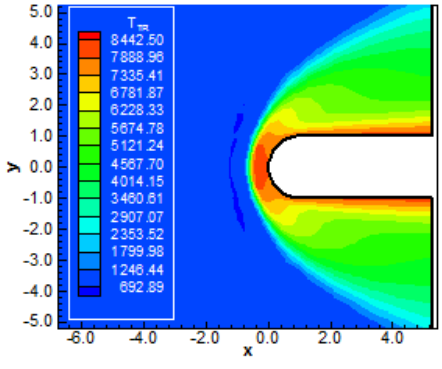

Figure 33: Temperature contours (CGL-C97)

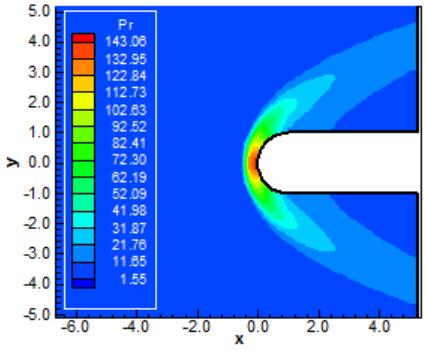

Figure 34: Pressure contours (LGR-C97)

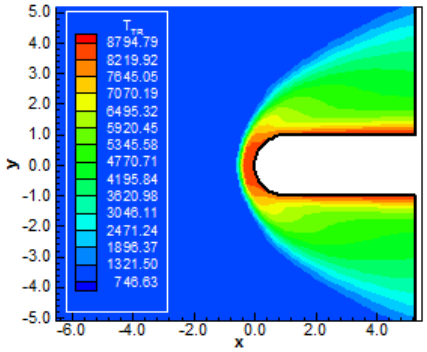

Figure 35: Temperature contours (LGR-C97)

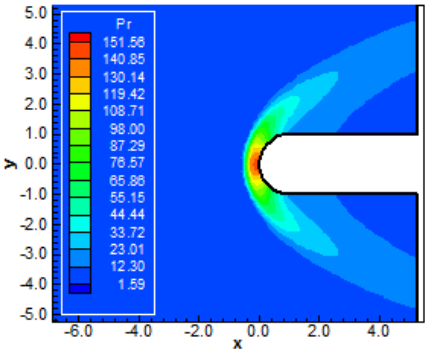

Figure 36: Pressure contours (LGL-C97)

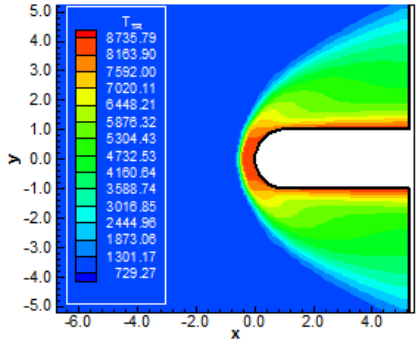

Figure 37: Temperature contours (LGL-C97)

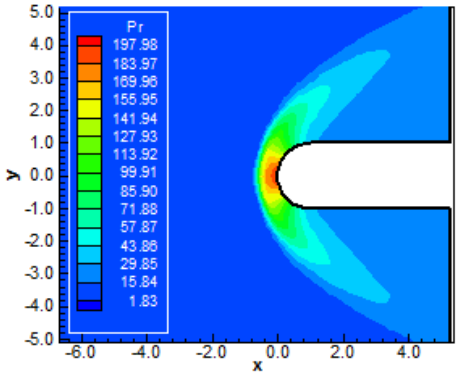

Figure 38: Pressure contours (CGR-RGYB98)

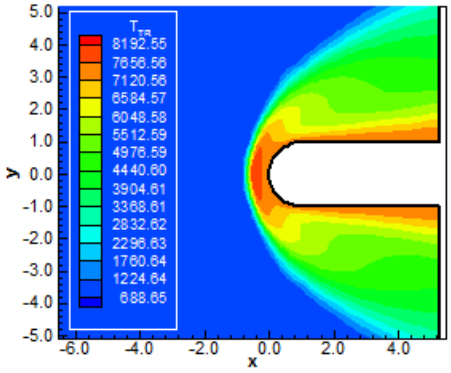

Figure 39: Temperature contours (CGR-RGYB98)

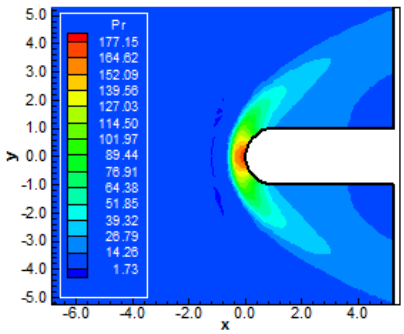

Figure 40: Pressure contours (CGL-RGYB98)

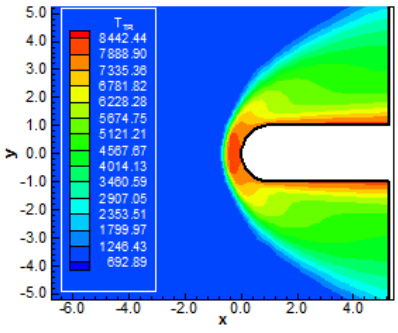

Figure 41: Temperature contours (CGL-RGYB98)

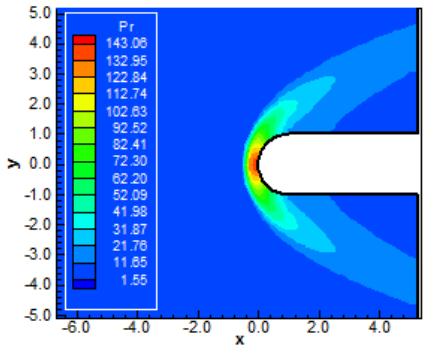

Figure 42: Pressure contours (LGR-RGYB98)

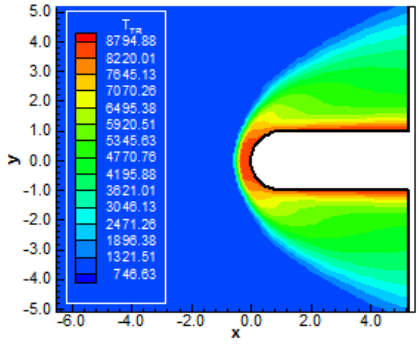

Figure 43: Temperature contours (LGR-RGYB98)

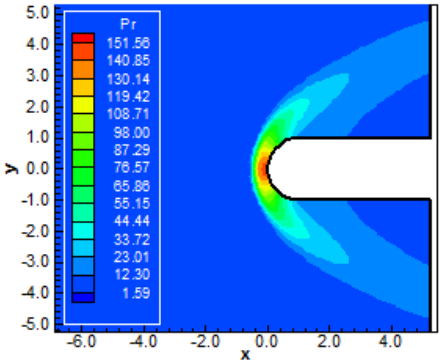

Figure 44: Pressure contours (LGL-RGYB98)

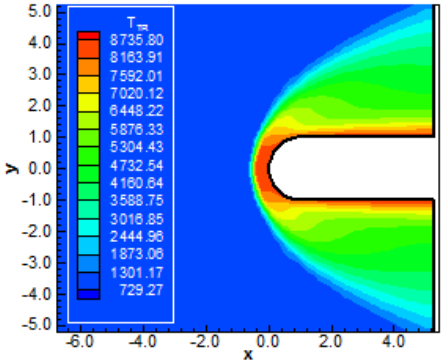

Figure 45: Temperature contours (LGL-RGYB98)

REENTRY CAPSULE TURBULENT SOLUTIONS – 16th ORDER

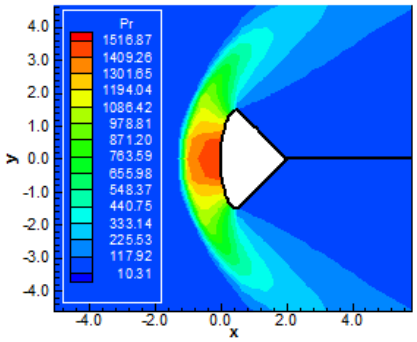

Figure 46: Pressure contours (CGR-C83)

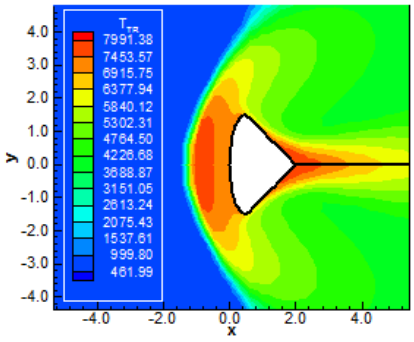

Figure 47: Temperature contours (CGR-C83)

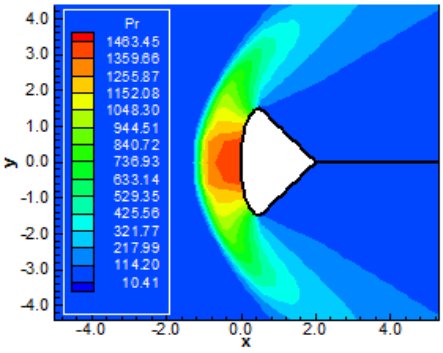

Figure 48: Pressure contours (CGL-C83)

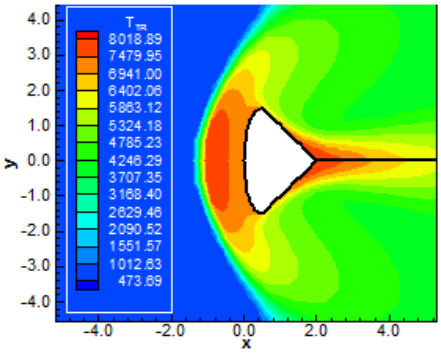

Figure 49: Temperature contours (CGL-C83)

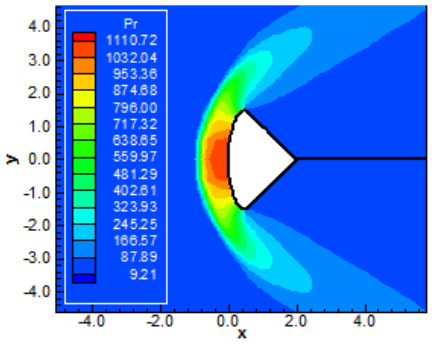

Figure 50: Pressure contours (LGR-C83)

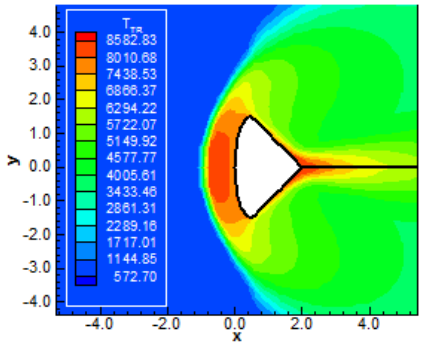

Figure 51: Temperature contours (LGR-C83)

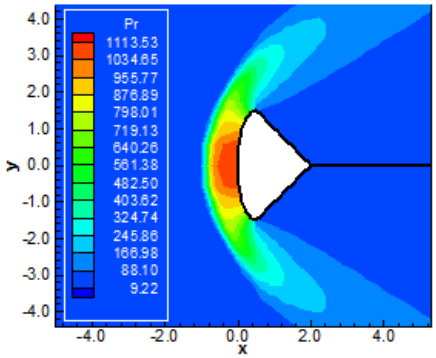

Figure 52: Pressure contours (LGL-C83)

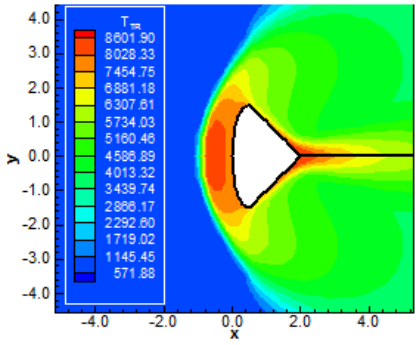

Figure 53: Temperature contours (LGL-C83)

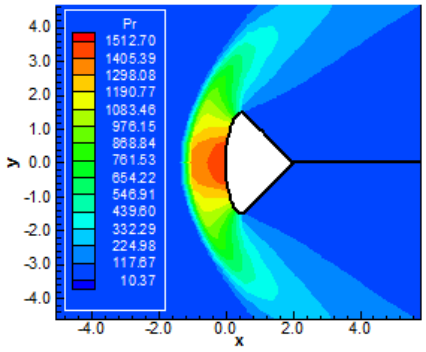

Figure 54: Pressure contours (CGR-W88)

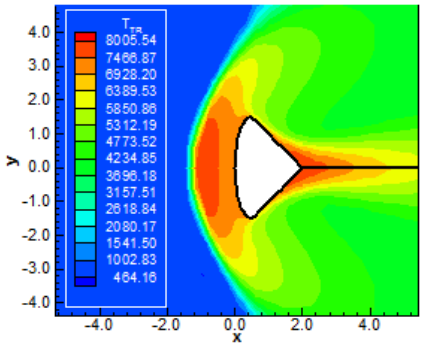

Figure 55: Temperature contours (CGR-W88)

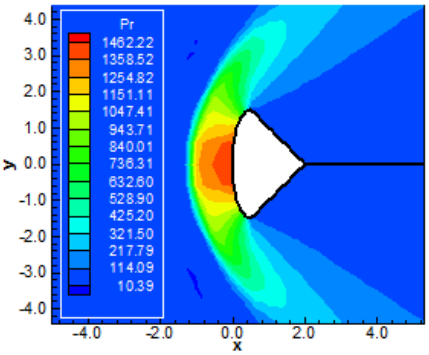

Figure 56: Pressure contours (CGL-W88)

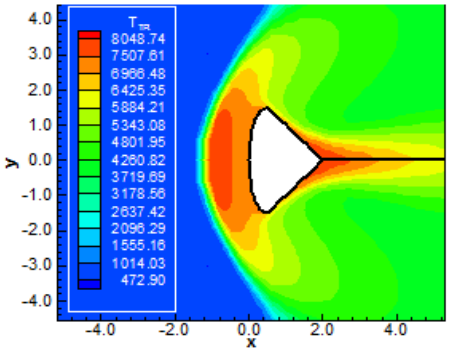

Figure 57: Temperature contours (CGL-W88)

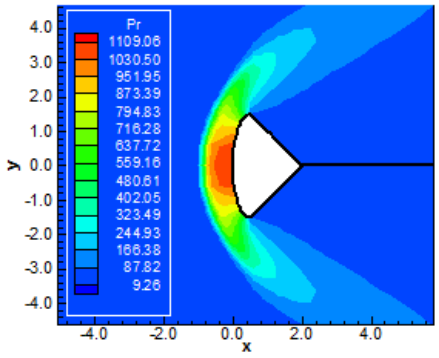

Figure 58: Pressure contours (LGR-W88)

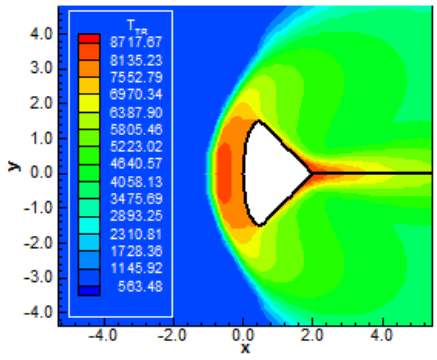

Figure 59: Temperature contours (LGR-W88)

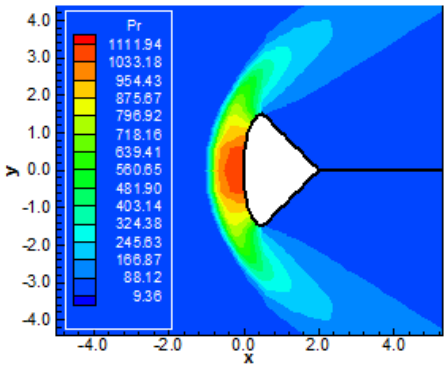

Figure 60: Pressure contours (LGL-W88)

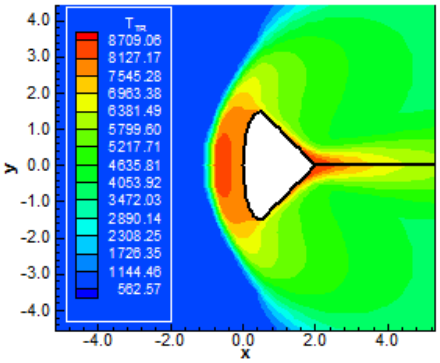

Figure 61: Temperature contours (LGL-W88)

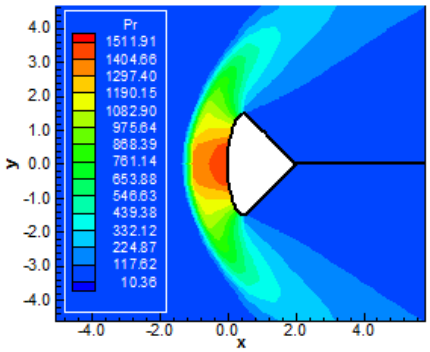

Figure 62: Pressure contours (CGR-YGO96)

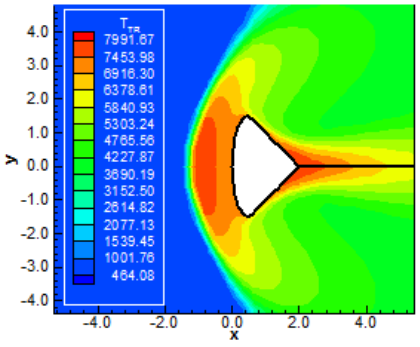

Figure 63: Temperature contours (CGR-YGO96)

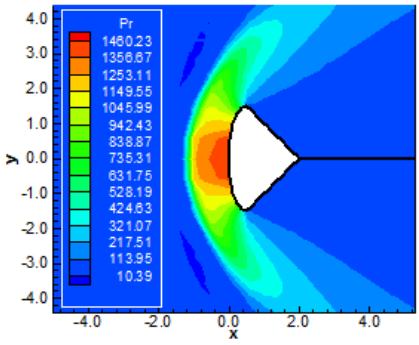

Figure 64: Pressure contours (CGL-YGO96).

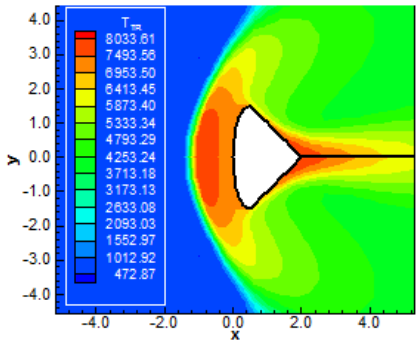

Figure 65: Temperature contours (CGL-YGO96)

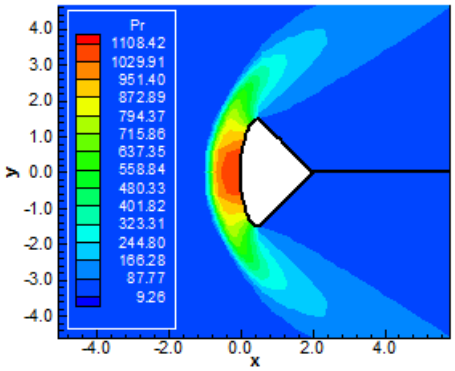

Figure 66: Pressure contours (LGR-YGO96)

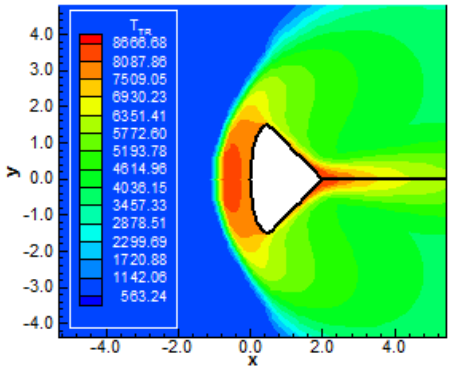

Figure 67: Temperature contours (LGR-YGO96)

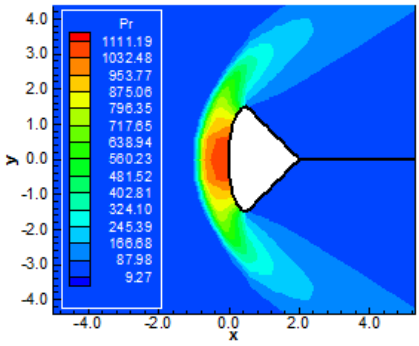

Figure 68: Pressure contours (LGL-YGO96)

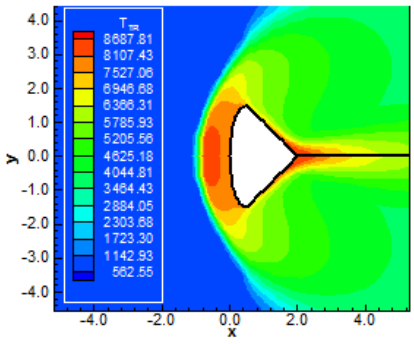

Figure 69: Temperature contours (LGL-YGO96)

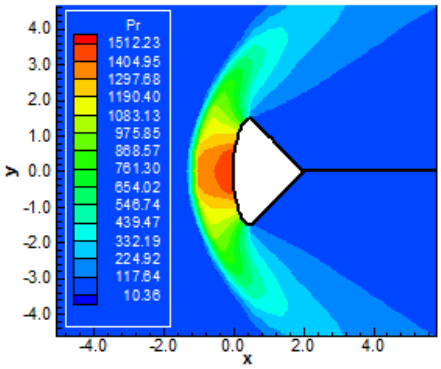

Figure 70: Pressure contours (CGR-C97)

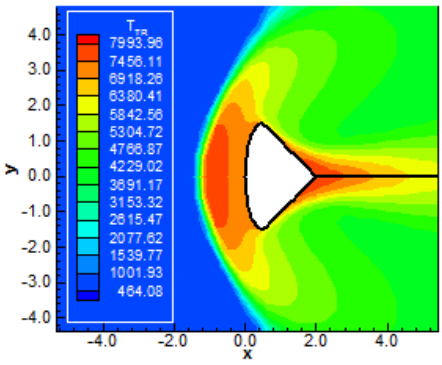

Figure 71: Temperature contours (CGR-C97)

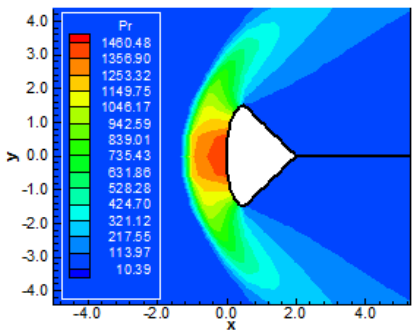

Figure 72: Pressure contours (CGL-C97)

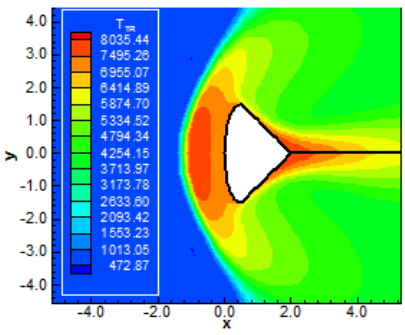

Figure 73: Temperature contours (CGL-C97)

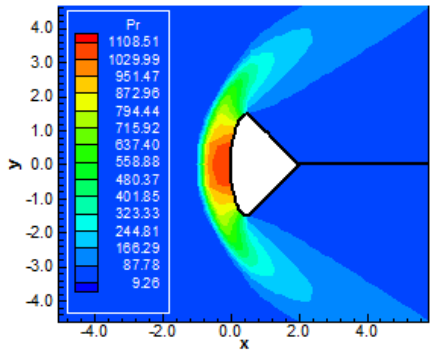

Figure 74: Pressure contours (LGR-C97)

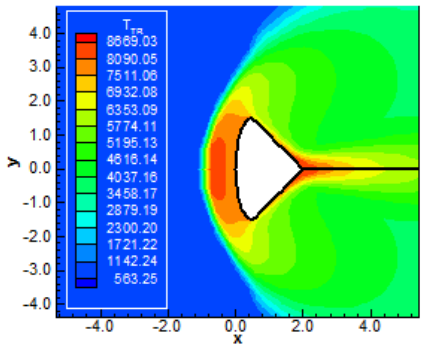

Figure 75: Temperature contours (LGR-C97)

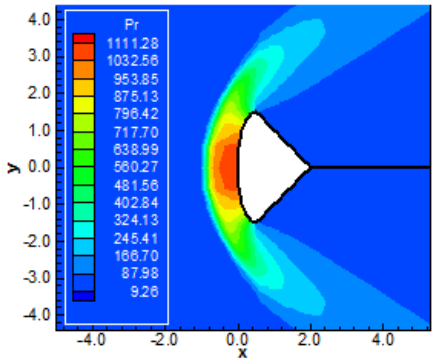

Figure 76: Pressure contours (LGL-C97)

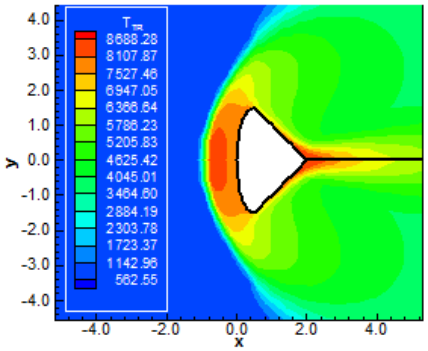

Figure 77: Temperature contours (LGL-C97)

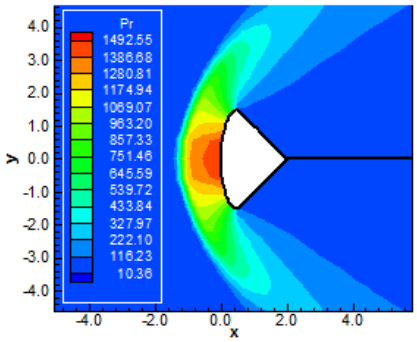

Figure 78: Pressure contours (CGR-RGYB98)

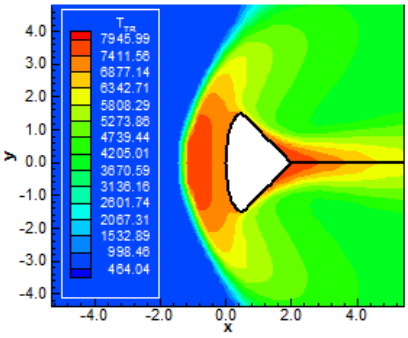

Figure 79: Temperature contours (CGR-RGYB98)

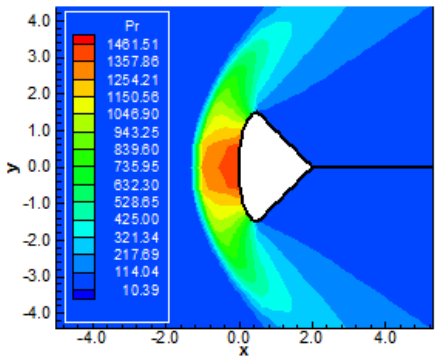

Figure 80: Pressure contours (CGL-RGYB98)

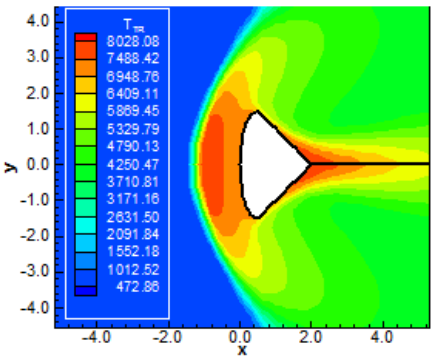

Figure 81: Temperature contours (CGL-RGYB98)

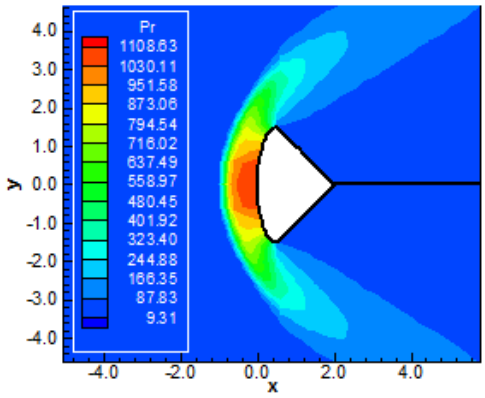

Figure 82: Pressure contours (LGR-RGYB98)

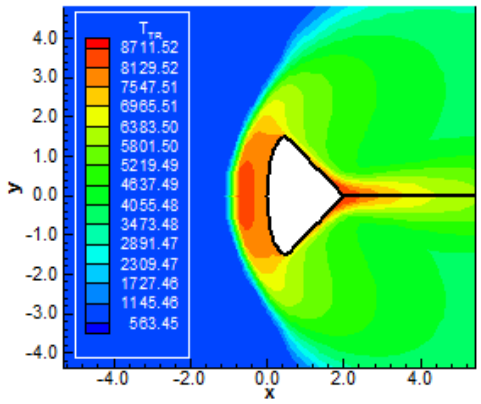

Figure 83: Temperature contours (LGR-RGYB98)

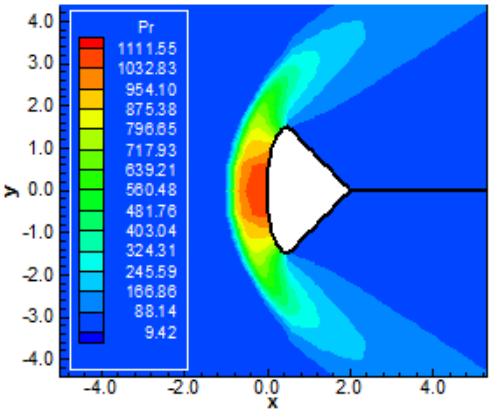

Figure 84: Pressure contours (LGL-RGYB98)

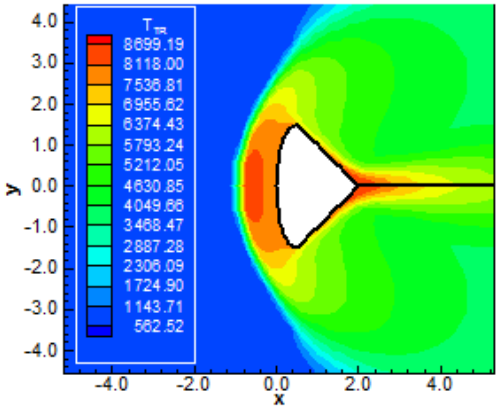

Figure 85: Temperature contours (LGL-RGYB98)

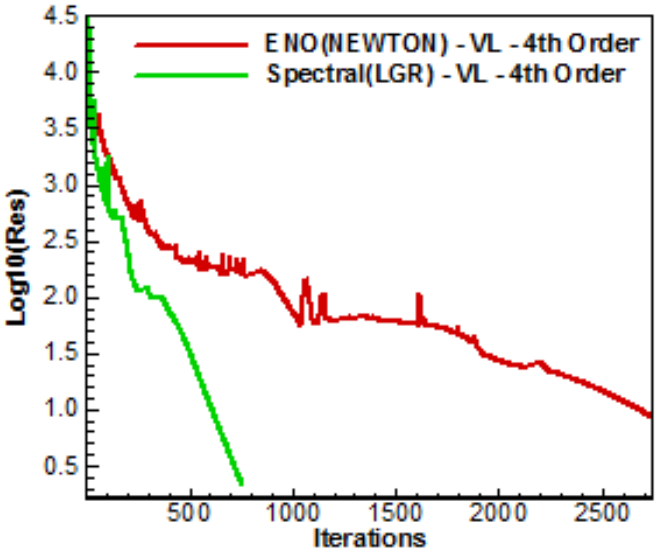

Figure 86: Convergence histories

11. Conclusions

This work analyzed a spectral method applied to the Favre-averaged Navier-Stokes equations in two-dimensions, employing a structured spatial discretization, and using a conservative and finite volume approaches. Turbulence was taken into account considering the implementation of five k-ω two-equation

turbulence models, based on the works of [19-23]. The numerical experiments were performed using the [24] numerical algorithm. The Euler backward method was applied to march the scheme in time. The spectral method presented in this work employed collocation points and variants of Chebyshev and Legendre interpolation functions were analyzed. Chemical non-equilibrium was studied using a five species chemical model. The "hot gas" hypersonic flows around a blunt body, and around a reentry capsule, in two-dimensions, were simulated. The results have indicated that the Chebyshev collocation point variants were more accurate in terms of stagnation pressure estimations. In the blunt body problem such errors were inferior to 16.0%, being 2.66% the best result, while in the reentry capsule problem such errors were inferior to 8.0%, being 3.88% the best result. The Legendre collocation point variants were more accurate in terms of the lift coefficient estimations. Moreover, the Legendre collocation point variants were more computationally efficient and cheaper.

As final conclusion, it is possible to highlight that, for the blunt body problem, the [24] scheme coupled with the [19] turbulence model using Chebyshev-Gauss-Lobatto collocation points had the best performance in estimating the stagnation pressure, and the lift aerodynamic coefficient was better estimated by the [24] scheme as using the Legendre-Gauss-Radau collocation points also coupled with the [19] turbulence model; and for the reentry capsule problem, the [24] scheme coupled with the [21] turbulence model using Chebyshev-Gauss-Lobatto collocation points had the best performance in estimating the stagnation pressure, and the lift aerodynamic coefficient was better estimated by the [24] scheme as using the Legendre-Gauss-Lobatto collocation points also coupled with the [19] turbulence model. Moreover, the best performance of the numerical scheme, for the 4^{th} order of accuracy, was coupled with the [19] turbulence model, when using the Legendre-Gauss-Radau collocation points, employing a CFL of 0.30, and converging in 754 iterations, whereas for the 16^{th} order of accuracy, the best performance of the numerical scheme was coupled with the [19] turbulence model, when using the Legendre-Gauss-Radau collocation points, employing a CFL of 0.30, and converging in 630 iterations.

Finally, to close this work, the computational cost of the numerical scheme using the several types of collocation points was presented in Tabs. 8-9. For the 4^{th} order of accuracy, the cheapest combination was the [24] scheme coupled with [20] turbulence model and using Legendre-Gauss-Lobatto collocation points with a cost of 0.0002292 sec/per-volume/per-iteration, whereas for the 16^{th} order of accuracy the cheapest was due to the [24] scheme coupled with the [21] turbulence model and using the Chebyshev-Gauss-Radau collocation points with a cost of 0.0005523 sec/per-volume/per-iteration.

References

[1]. Barnes CJ, Huang GP, Shang JS. A high resolution spectral method for the compressible Navier-Stokes equations. AIAA Paper 2011-0049; 2011.

[2]. Huang P, Wang ZJ, Liu Y. An implicit space-time spectral difference method for discontinuity capturing using adaptive polynomials. AIAA Paper 2005-5255; 2005.

[3]. Huang P. High order discontinuity capturing using adaptive polynomials. AIAA paper 2006-0305; 2006.

[4]. Steger JL, Warming RF. Flux vector splitting of the inviscid gasdynamic equations with application to finite difference methods. Journal of Computational Physics, 1981; 40: 263-293.

[5]. Hughes T. The finite element method, linear static and dynamic finite element analysis. Prentice-Hall, Inc.

[6]. Lele S. Compact finite difference schemes with spectral-like resolution. Journal of Computational Physics, 1991; 103: 16-42.

[7]. Gottlieb D, Orszag S. Numerical analysis of spectral methods: theory and applications. Society for Industrial and Applied Mathematics, Philadelphia.

[8]. Hussaini MY, Kopriva DA, Salas MD, Zang TA. Spectral methods for the Euler equations: Part I – Fourier methods and shock capturing. AIAA Journal, 1985; 23(1): 64-70.

[9]. Slater JC. Electronic energy bands in metal. Physical Review, 1934; 45: 794-801.

[10]. Barta J. Ü ber die naherungsweise l ü sung einigerzweidimensionalerelastizit ä tsaufgaben. Zeitschrift fuer Angewandte Mathematik und Mechanik, 1937; 17: 184-185.
[11]. Frazer RA, Jones WP, Skan SW. Approximation to functions and to the solutions of differential equations. Aeronautical Research Council, London. R&M 1799; 1937.
[12]. Lanczos CL. Trigonometric interpolation of empirical and analytic functions. Journal of Mathematics and Physics, 1938; 17: 123-199.
[13]. Gottlieb D, Lustman L, Orszag SA. Spectral calculations of one-dimensional inviscid compressible flows. SIAM Journal of Scientific and Statistical Computation, 1981; 2: 296-310.
[14]. Taylor TD, Meyers RB, Albert JH. Pseudospectral calculations of shock waves, rarefaction waves and contact surfaces. Computers and Fluids, 1981; 9: 469-473.
[15]. Zang TA, Hussaini MY. Mixed spectral-finite difference approximations for slightly viscous flows. Proceedings of the 7th International Conference on Numerical Methods in Fluid Dynamics. Edited by W. C. Reynolds and R. W. MacCormack. Lecture Notes in Physics, Springer-Verlag, New York, 1981; (141): 461-466.
[16]. Narayan JR, Girimaji SS. Turbulent reacting flow computations including turbulence-chemistry interactions. AIAA Paper 92-0342; 1992.
[17]. Gnoffo PA, Gupta RN, Shinn JL. Conservation equations and physical models for hypersonic flows in thermal and chemical nonequilibrium. NASA TP 2867; 1989.
[18]. Liu M, Vinokur M.Upwind algorithms for general thermo-chemical nonequilibrium flows. AIAA Paper 89-0201; 1989.
[19]. Coakley TJ. Turbulence modeling methods for the compressible Navier-Stokes equations. AIAA Paper 83-1693; 1983.
[20]. Wilcox DC. Reassessment of the scale-determining equation for advanced turbulence models. AIAA Journal, 1988; 26(11): 1299-1310.
[21]. Yoder DA, Georgiadids NJ, Orkwis PD. Implementation of a two-equation k-omega turbulence model in NPARC.AIAA Paper 96-0383; 1996.
[22]. Coakley TJ. Development of turbulence models for aerodynamic applications.AIAA Paper 97-2009; 1997.
[23]. Rumsey CL, Gatski TB, Ying SX, Bertelrud A. Prediction of high-lift flows using turbulent closure models. AIAA Journal, 1998; 36(5): 765-774.
[24]. Van Leer B. Flux-vector splitting for the Euler equations. Lecture Notes in Physics, Springer Verlag, Berlin, 1982; 170: 507-512.
[25]. Maciel ESG. Simulations in 2D and 3D Applying Unstructured Algorithms, Euler and Navier-Stokes Equations – Perfect Gas Formulation. Saarbrücken, Deutschland: Lambert Academic Publishing (LAP), 2015; Ch. 1: 26-47.
[26]. Maciel ESG. Simulations in 2D and 3D Applying Unstructured Algorithms, Euler and Navier-Stokes Equations – Perfect Gas Formulation. Saarbrücken, Deutschland: Lambert Academic Publishing (LAP), 2015; Ch. 6: 160-181.
[27]. Saxena SK, Nair MT. An improved Roe scheme for real gas flow. AIAA Paper 2005-0587; 2005.
[28]. Hussaini MY, Streett CL, Zang TA. Spectral methods for partial differential equations. ICASE Report No. 83-46; 1983.
[29]. Davis PA, Rabinowitz P. Numerical Integration. Blaisdell Publishing Co.; 1967.
[30]. Canuto C, Hussaini MY, Quarteroni A, Zang TA. Spectral methods evolution to complex geometries and applications to fluid dynamics. Scientific Computation Springer, 2007.
[31]. Narayan JR. Computation of compressible reacting flows using a two-equation turbulence model. Proceedings of the 4th International Symposium on Computational Fluid Dynamics, Davis, California, September, 1991.
[32]. Williams FA. Combustion Theory. Addison-Wesley Publishing Company, Inc., Reading, MA, 1965.
[33]. Drummond JP, Carpenter MH, Riggins DW. Mixing and mixing enhancement in supersonic reacting flows.High Speed Propulsion Systems: Contributions to Thermodynamic Analysis. Edited by E. T.

Curran and S. N. B. Murthy. American Institute of Astronautics and Aeronautics (AIAA), Washington, D. C., 1990.
[34]. Maciel ESG. Pimenta AP. Chemical non-equilibrium reentry flows in two-dimensions – Part I. WSEAS Transactions on Fluid Mechanics, 2013; 8(1): 1-20.
[35]. Maciel ESG. Pimenta AP. Chemical non-equilibrium reentry flows in two-dimensions – Part II. WSEAS Transactions on Fluid Mechanics, 2013; 8(2): 50-79.
[36]. Maciel ESG. Hypersonic reactive flow simulations in two-dimensions, chemical and thermochemical non-equilibrium conditions. Saarbrücken. Deutschland: Lambert Academic Publishing (LAP), 2015; Ch. 1: 27-81.
[37]. Maciel ESG. Hypersonic reactive flow simulations in two-dimensions, chemical and thermochemical non-equilibrium conditions. Saarbrücken. Deutschland: Lambert Academic Publishing (LAP), 2015; Ch. 2: 82-173.
[38]. Favre A. Statistical equations of turbulent gases. Institut de Mechanique Statistique de la Turbulence, Marseille.
[39]. Maciel ESG. Turbulent thermochemical non-equilibrium reentry flows in 2D.Computational and Applied Mathematics Journal, 2015; 1(4): 201-224.
[40]. Maciel ESG, Andrade, CR. Turbulent thermochemical non-equilibrium reentry flows in 2D – Eleven species. Asian Journal of Mathematics and Computer Research, 2017; 20(4): 179-217.
[41]. Prabhu RK. An implementation of a chemical and thermal nonequilibrium flow solver on unstructured meshes and application to blunt bodies. NASA CR-194967; 1994.
[42]. Ait-Ali-Yahia D, Habashi WG. Finite element adaptive method for hypersonic thermochemical nonequilibrium flows. AIAA Journal, 1997; 35(8): 1294-1302.
[43]. Radespiel R, Kroll N. Accurate flux vector splitting for shocks and shear layers. Journal of Computational Physics, 1995; 121: 66-78.
[44]. Long LN, Khan MMS, Sharp HT. Massively parallel three-dimensional Euler / Navier-Stokes method.AIAA Journal, 1991; 29(5): 657-666.
[45]. Fox RW, McDonald AT. Introdução à mecânica dos fluidos. Guanabara Editor, 1988.
[46]. Maciel ESG. Simulação numérica de escoamentos supersônicos e hipersônicosutilizando técnicas de dinâmica dos fluidos computacional. Doctoral thesis, ITA, CTA, São José dos Campos, SP, Brazil, 2002.
[47]. Maciel ESG. High order resolution applied to chemical non-equilibrium reentry flows in 2D, Engineering and Technology, 2015; 2(5): 256-275.
[48]. Maciel ESG, Andrade CR. Turbulent chemical non-equilibrium reentry flows in 2D - Five species, Asian Journal of Mathematics and Computer Research, 2017; 20(3): 130-168.
[49]. Anderson Jr. JD. Fundamentals of aerodynamics, McGraw-Hill, Inc., 5th Edition, 1008p., 2010.